

## **TURBULENT FLOW SIMULATIONS IN BIFURCATED NOZZLES: EFFECTS OF DESIGN AND CASTING OPERATION**

Fady M. Najjar, Brian G. Thomas, and Donald E. Hershey<sup>†</sup>

### **ABSTRACT**

Bifurcated nozzles are used in continuous casting of molten steel, where they influence the quality of the cast steel slabs. The present study performs two and three-dimensional simulations of steady turbulent ( $K-\epsilon$ ) flow in bifurcated nozzles, using a finite-element (FIDAP) model, which has been verified previously with water model experiments. The effects of nozzle design and casting process operating variables on the jet characteristics exiting the nozzle are investigated. The nozzle design parameters studied include the shape, angle, height, width, and thickness of the ports and the bottom geometry. The process operating practices include inlet velocity profile and angle, and port curvature caused by erosion or inclusion buildup. Results show that the jet angle is controlled mainly by the port angle, but is steeper with larger port area and thinner walls. The degree of swirl is increased by larger or rounder ports. The effective port area, where there is no recirculation, is increased by smaller or curved ports. Flow asymmetry is more severe with skewed or angled inlet conditions or unequal port sizes. Turbulence levels in the jet are higher with higher casting speed and smaller ports.

<sup>†</sup> FADY M. NAJJAR, formerly Research Assistant, Department of Mechanical and Industrial Engineering, University of Illinois, Urbana, IL is with the National Center for Supercomputing Applications, University of Illinois, 5600 Beckman Institute, 405 North Mathews, Urbana, IL 61801. BRIAN G. THOMAS, Associate Professor, is with the Department of Mechanical and Industrial Engineering, University of Illinois, 1206 West Green St., Urbana, IL 61801. DONALD E. HERSHEY, formerly Research Assistant in the same department, is with G.E. Aircraft Engines, One Neumann Way, M.D. A106, Cincinnati, OH 45215.

## 1. INTRODUCTION

Hundreds of millions of tons of liquid metal flow through nozzles every year, during the processing of semi-finished metal products. The primary function of the nozzle is to protect the liquid metal from reoxidation during transfer between metallurgical vessels. In addition, the nozzle controls the flow pattern developed in the second vessel, since the nozzle governs the speed, direction and other characteristics of the liquid jet entering the vessel. The jet in turn influences the ultimate quality of the product through its effect on surface waves, heat and mass transfer.

The continuous casting mold for solidifying steel slabs is one example of a process where the nozzle plays a critical role. This process is important because, over the past decade, the fraction of steel produced in the United States via continuous casting has grown from 29% to over 67%.<sup>1</sup> Continued viability of the steel industry depends upon improved efficiency and consistent quality of steel production. Improving the “submerged entry nozzle”, or SEN, which controls the delivery of steel into the mold, is one step towards this goal.

A schematic of part of the continuous casting process is depicted in Figure 1, showing the tundish, SEN, and mold regions. Steel flows through a holding vessel called a “tundish”, and exits down through a ceramic SEN, and into a bottomless mold. In the mold, a thin layer of steel freezes against the water-cooled copper walls to form a solid “shell”. The solidifying shell grows as it is continuously withdrawn from the bottom of the mold at a rate or “casting speed”, that matches the flow of incoming liquid metal. Below the mold, the shell acts as a container to support the “pool” of molten steel. Additional cooling of the shell surface is provided by water sprays. A layer of “mold powder”, composed mainly of silica and metal oxides, protects the top surface of the liquid steel in the mold. The solid powder melts to form a liquid “mold flux layer”, which feeds between the shell and the mold walls at the “meniscus”, where it acts as a lubricant.

Flow through the SEN is gravity-driven by the pressure difference between the liquid levels of the tundish and mold top free surfaces. Thus, the flow rate depends upon the amount of steel in the tundish and the flow characteristics inside the SEN. The flow rate of molten steel is controlled to maintain a constant liquid level in the mold in several ways. The most popular mechanism is a “slide gate” that blocks off a portion of the SEN pipe section by moving a disk-shaped plate through a horizontal slit across the entire SEN, as pictured in Figure 1. This flow adjustment method allows for independent control of casting speed and metal level, and is also essential for stopping the flow of molten steel when the operation must be terminated abruptly.

The SEN has an important influence on steel quality through its effect on the flow pattern in the mold. The SEN should deliver steel uniformly into the mold while preventing problems such as surface waves, meniscus freezing and crack formation. Impingement of hot liquid metal with high momentum against the solidifying shell can contribute to shell thinning and even costly “breakouts”, where liquid steel bursts from the shell.<sup>2, 3</sup> Flotation of detrimental alumina inclusions into the protective molten slag layer can be enhanced by an appropriate flow pattern inside the mold. Plant experience has found that many serious quality problems are directly associated with SEN operation and the flow pattern in the mold.<sup>4</sup> For example, surface waves and turbulence near the top free surface can entrain some of the slag or gas bubbles into the steel, causing dangerous large inclusions and surface slivers<sup>4</sup>. Finally, clogging due to inclusion buildup on the SEN walls redirects the flow through the SEN, and hence, affects the jet characteristics exiting from the SEN ports. As a result, the ports are usually oversized to accommodate some clogging before the flow becomes constricted.

This study investigates the application of two and three-dimensional finite-element models, using the K- $\epsilon$  turbulence equations, for the prediction of flow through a typical SEN. This particular nozzle configuration, shown in Figure 2, is symmetrical and bifurcated, with two opposing rectangular exit ports (180° apart), which is typical of the nozzles used in the continuous casting of steel slabs. There is great incentive to understand and predict the flow through this nozzle because the SEN geometry is one of the few variables that is both very influential on the process and relatively inexpensive to change.

Past experimental work to understand how SEN design affects flow in the mold and associated phenomena has been performed primarily using water models of the SEN and mold.<sup>4, 5, 6, 7, 8, 9</sup> This approach is recently being supplemented by numerical studies. Successful applications of finite-difference models to continuous casting include the prediction of the flow pattern in the mold combined with heat transfer,<sup>2</sup> particle trajectories,<sup>10</sup> electromagnetic motion<sup>11, 12</sup> and free-surface movement<sup>13</sup>. The complex geometry of the SEN is more easily modeled using the finite-element method.<sup>14, 15</sup> Two-dimensional finite-element models have been developed to explore the effect of process variables on flow in the SEN and the mold.<sup>15, 16, 17, 18</sup> Further, Wang<sup>19</sup> investigated the effect of slide gate position on asymmetrical flow through the SEN ports using a 3-D finite-element model. Yao<sup>20</sup> used a finite-volume method to model flow through the SEN and the mold together.

The goal of the present work is to develop and assess the accuracy of a 3-D finite-element simulation in predicting the flow pattern through a typical SEN used in the continuous casting of

steel slabs. The commercial code FIDAP<sup>21</sup> was chosen because it is a popular, well-supported, finite-element code that has been found in previous work to be reasonably accurate.<sup>16, 22</sup> The predictions are compared with observations and measurements made on a water model. Results and computational requirements of a 2-D simulation are then evaluated with the 3-D calculations. Two-dimensional simulations of the SEN and the mold are further performed to investigate the effect of the SEN outlet boundary conditions on the characteristics of the jet exiting the SEN.

This work represents a preliminary step of a larger systematic study of the many SEN design parameters such as port angle, width, thickness and height, and well design. The results will be useful for understanding and preventing problems associated with SEN operation and assisting in the design of new SENs for the continuous casting process. They should also be of general interest for other processes involving turbulent flow through bifurcated nozzles with oversized ports, and for other numerical studies of turbulent flow using 3-D finite-element calculations.

## 2. MODEL FORMULATION

### 2.1 Governing Equations

The flow of molten steel through the SEN has a Reynolds number of 95,300 in the pipe section, and hence is three-dimensional, highly turbulent, and time dependent in nature. The time-mean velocities,  $\overline{v_i} = \{ \overline{v_x}, \overline{v_y}, \overline{v_z} \}$ , and pressure,  $\overline{p}$ , are calculated by solving the 3-D, incompressible, steady-state, isothermal mass and momentum conservation equations for a Newtonian fluid:

$$\frac{\partial \overline{v_i}}{\partial x_i} = 0 \quad (1)$$

$$\rho \left( \overline{v_j} \frac{\partial \overline{v_i}}{\partial x_j} \right) = - \frac{\partial \overline{p}}{\partial x_i} + \rho \overline{f_i} + \frac{\partial}{\partial x_j} \left[ \mu \left( \frac{\partial \overline{v_i}}{\partial x_j} + \frac{\partial \overline{v_j}}{\partial x_i} \right) \right] \quad (2)$$

where  $\overline{f_i}$  represents body forces,  $\rho$  is density,  $\mu$  is viscosity, and  $\{i, j\} = \{1, 2, 3\}$  in the Cartesian system  $\{x_1, x_2, x_3\} = \{x, y, z\}$ , and repeated indices indicate summation. Since the flow is turbulent, a turbulence model is needed to close the system of equations. The standard, two-equation K- $\epsilon$  model is chosen, requiring the solution of two additional transport equations to find the turbulent kinetic energy, K, and turbulent dissipation,  $\epsilon$ , fields.<sup>23</sup> These equations are given by:

$$\rho \left( \overline{v_j} \frac{\partial K}{\partial x_j} \right) = \frac{\partial}{\partial x_j} \left( \frac{\mu_t}{\sigma_k} \frac{\partial K}{\partial x_j} \right) + \mu_t \Phi - \rho \varepsilon \quad (3)$$

$$\rho \left( \overline{v_j} \frac{\partial \varepsilon}{\partial x_j} \right) = \frac{\partial}{\partial x_j} \left( \frac{\mu_t}{\sigma_\varepsilon} \frac{\partial \varepsilon}{\partial x_j} \right) + c_1 \frac{\varepsilon}{K} \mu_t \Phi - c_2 \rho \frac{\varepsilon^2}{K} \quad (4)$$

where

$$\Phi = \frac{\partial \overline{v_j}}{\partial x_i} \left( \frac{\partial \overline{v_i}}{\partial x_j} + \frac{\partial \overline{v_j}}{\partial x_i} \right) \quad (5)$$

Equations (1-5) represent the time averaged, velocity field and employ the Boussinesq concept for modeling the turbulent stresses:

$$-\rho \overline{v'_i v'_j} = \mu_t \left( \frac{\partial \overline{v_i}}{\partial x_j} + \frac{\partial \overline{v_j}}{\partial x_i} \right) \quad (6)$$

where  $v'_i$  is the fluctuating component of the velocity. The viscosity,  $\mu$ , in equation (2) is composed of two components:

$$\mu = \mu_o + \mu_t \quad (7)$$

where  $\mu_o$  is the molecular viscosity and  $\mu_t$  the turbulent (or eddy) viscosity which accounts for the turbulent nature of the flow. The turbulent viscosity is calculated from the turbulent kinetic energy and dissipation by:

$$\mu_t = C_\mu \rho \frac{K^2}{\varepsilon} \quad (8)$$

The above equations contain five empirical constants that appear to produce reasonable behavior for a wide range of flows<sup>24, 25</sup> when given standard values as follows:

$$C_1 = 1.44 \quad C_2 = 1.92 \quad C_\mu = 0.09 \quad \sigma_k = 1.00 \quad \sigma_\varepsilon = 1.30$$

The above set of equations, equations (1-8), contains 6 unknown variables  $\overline{v_i}$ ,  $\overline{p}$ ,  $K$ , and  $\varepsilon$ . Gravity forces, such as caused by thermal-solutal buoyancy, have been neglected and single phase flow has been assumed.

## 2.2 Solution Methodology

The governing equations (1-5) were discretized using the finite-element method and solved with the FIDAP code, version 6.01.<sup>21</sup> The continuity equation, equation (1), was satisfied using the penalty function approach<sup>21</sup>

$$\frac{\partial \overline{v_i}}{\partial x_i} = -\sigma \overline{p} \quad (9)$$

where  $\sigma$  is a small constant, chosen here to be  $10^{-8}$ .

The computational domain is subdivided into discrete regions called elements. The dependent variables,  $\overline{v_i}$ ,  $\overline{p}$ ,  $\mathbf{K}$ , and  $\varepsilon$ , are approximated in each element in terms of nodal values using interpolation “shape” functions as follows:

$$\begin{aligned} \overline{v_i}(\mathbf{x}) &= \Phi^T \mathbf{V}_i \\ \overline{p}(\mathbf{x}) &= \Psi^T \mathbf{P} \\ \mathbf{K}(\mathbf{x}) &= \Phi^T \mathbf{K} \\ \varepsilon(\mathbf{x}) &= \Phi^T \mathbf{E} \end{aligned} \quad (10)$$

where  $\mathbf{V}_i$ ,  $\mathbf{P}$ ,  $\mathbf{K}$ ,  $\mathbf{E}$  are column vectors of element nodal point unknowns,  $\Phi$  and  $\Psi$  are column vectors of interpolation functions. Substituting equation (10) into the governing equations (1-4) yields sets of residuals (errors). Applying Galerkin's method, the residuals are made orthogonal to the shape functions, thereby setting the weighted average error over the entire domain to zero.<sup>21</sup> Assembly of the resulting equations integrated numerically over each element produces a global system of nonlinear algebraic equations expressed as:

$$[S(u)] \cdot \{u\} = \{F\} \quad (11)$$

where  $[S(u)]$  is the stiffness matrix,  $\{u\} = \{ \overline{V_x}, \overline{V_y}, \overline{V_z}, \overline{V}, \mathbf{K}, \mathbf{E} \}^T$  and  $\{F\}$  is the force vector. Equation (11) is solved for  $\{u\}$  using a relaxed successive substitution scheme:

$$[S(u^{i-1})] \cdot \{u^*\} = \{F\} \quad (12)$$

$$\{u^{i+1}\} = RF \{u^*\} + (1-RF) \{u^i\} \quad (13)$$

where RF is a relaxation factor,  $0 \leq \text{RF} \leq 1$ , and the superscripts refer to the iteration level. Further details are given in the FIDAP manual.<sup>20</sup>

This formulation solves the discretized equation, equation (11), in a fully coupled manner, which requires a computationally intensive out-of-core scheme when the mesh size is too large. A segregated solver, based on decoupling the six unknowns in equation (11), requires an order of magnitude less internal memory storage (RAM) to run in-core and runs about 3 times faster per iteration. However, the rate of convergence of the segregated solver is very slow; it takes roughly ten times more iterations to converge than the fully-coupled solver. Thus, the direct solver is deemed to be more efficient for the present simulations, which are sufficiently small enough to run in-core.

The present simulations activated a Petrov-Galerkin formulation, or streamline upwinding.<sup>21</sup> This could introduce some false diffusion and has been reported to affect the flow in low velocity regions of the computational domain.<sup>22</sup> Without upwinding, however, the solution becomes highly unstable and it is extremely difficult to converge to any solution at all.

### **3. 3-D SEN MODEL**

The governing discretized equations are solved in the domain of a typical SEN, such as those currently used at Inland Steel. Figure 2 shows a schematic of this SEN and Table 1 summarizes the standard dimensions and operating conditions used in this study. For the 3-D simulation, two-fold symmetry is exploited to reduce the computer requirements. Two vertical symmetry planes parallel to the central axis are taken through the center-plane of the SEN and the middle of the ports. With these symmetry planes, only one quarter of the SEN need be modeled. To further reduce the number of elements, only the bottom 0.3 m of the 0.5-m SEN is simulated. The 3-D finite-element mesh consists of 5415 nodes, 4432 eight-node, linear, brick elements and 802 eight-node near-wall elements. The near-wall elements account for the transition from the turbulent boundary layer to the wall surfaces and are discussed below. Figure 3 illustrates the mesh for the standard 90 x 60 mm<sup>2</sup>, 15° down SEN studied in this work. Also shown are the applied boundary conditions for the 3-D SEN simulations.

#### ***3.1 Symmetry Planes and Outlet Boundary Conditions***

The component of velocity normal to the symmetry planes are fixed to zero to prevent fluid from penetrating the surface. The normal gradients of the two remaining velocity components, the turbulent kinetic energy, and the turbulent dissipation, are set to zero. These stress-free boundary conditions are also applied to all variables on the outlet plane of the port.

### 3.2 Wall Surfaces

Since the k-ε turbulent model is of the high Reynolds number type, it can not be applied in the near-wall regions. To overcome this constraint, the law-of-the-wall approach has been extensively used in numerical flow simulations. In the present work, near-wall elements are created along all wall surfaces to capture the steep gradients in the near-wall region without using excessive mesh refinement. These elements employ special shape functions, based on Reichardt's law.<sup>26</sup> The four interpolating shape functions, which comprise  $\Phi$  in equation (10) for a four-node (2-D) near-wall element, are:

$$\Phi(t,n) = \begin{bmatrix} T_1(t) \cdot N_1(n) \\ T_2(t) \cdot N_1(n) \\ T_1(t) \cdot N_2(n) \\ T_2(t) \cdot N_2(n) \end{bmatrix} \quad (14)$$

where t and n represent the coordinate directions tangential and normal to the wall, respectively; and T and N are the corresponding one-dimensional basis shape functions expressed as :

$$-1 \leq t \leq 1 ; T_1(t) = \frac{1}{2} (1-t) ; T_2(t) = \frac{1}{2} (1+t) \quad (15a)$$

$$-1 \leq n \leq 1 ; N_1(n) = 1 - \frac{A(n)}{A(n=1)} ; N_2(n) = \frac{A(n)}{A(n=1)} \quad (15b)$$

$$A(n) = \frac{1}{\kappa} \ln[1+0.2\Delta_u^+(1+n)] + 7.8 \left[ 1 - \exp\left(-\frac{\Delta_u^+(1+n)}{22}\right) - \frac{\Delta_u^+(1+n)}{22} \exp(-0.165\Delta_u^+(1+n)) \right] \quad (15c)$$

In equation (15c),  $\Delta_u^+$  is the dimensionless characteristic height of the element in the n-direction defined as :

$$\Delta_u^+ = \frac{\rho c_\mu^{0.25} K^{0.5} \Delta}{\mu_o} \quad (16)$$

where  $\Delta$  is the near-wall element height in the n-direction and  $K$  is the turbulent kinetic energy at the top of the element ( $n=+1$ ).

To ensure a proper implementation of these elements, the near-wall element top edges should lie beyond the viscous sub-layer, so the mesh was constructed with  $\Delta = 3.8$  mm to satisfy the condition,  $\Delta_u^+ > 30$ . Velocity components at the wall side ( $n=-1$ ) of these near-wall elements are set to zero to represent the stationary surfaces.

Boundary conditions on  $K$  and  $\varepsilon$  are applied at the top ( $n=+1$ ) of the near-wall elements as follows:

$$\frac{\partial K}{\partial n} = 0 \quad (17)$$

$$\varepsilon = \frac{(c_\mu^{0.5} K)^{1.5}}{\kappa \Delta} \quad (18)$$

where  $\kappa$  is the von-Karman constant with a value of 0.41. Since  $K$  and  $\varepsilon$  are not defined within these elements, an alternate formulation for  $\mu_t$  is required for the velocity solution, chosen to be the van Driest's mixing length model:

$$\mu_t = \rho l_m \left( \frac{\partial \bar{v}_i}{\partial x_j} \left( \frac{\partial \bar{v}_i}{\partial x_j} + \frac{\partial \bar{v}_j}{\partial x_i} \right) \right)^{1/2} \quad (19)$$

where 
$$l_m = \kappa \Delta \left( 1 - \exp(-\Delta_u^+/26) \right) \quad (20a)$$

Further details on this near-wall element formulation and the extension to 3-D are given elsewhere.<sup>21, 26</sup>

### 3.3 Inlet Boundary Conditions

The velocity, turbulent kinetic energy, and turbulent dissipation are specified at the inlet to the SEN. A uniform velocity profile in the z-direction was employed since it reasonably approximates the 1/7 power-law turbulent profile expected in pipe flow away from the walls. Other velocity components are set to zero, so that swirling is ignored. Turbulent kinetic energy and dissipation take the average values of the profiles calculated from a mixing-length model for turbulent pipe flow.<sup>27, 28</sup> Further details are described elsewhere.<sup>18</sup>

### 3.4 Computational Details

A solution strategy employing successive substitution requires approximately 25 iterations with a relaxation factor, RF, of 0.7 during the initial iterations, and 0.85 in later iterations. This achieves convergence of the solution vector to less than 1.2% error for velocities, and less than 3.0% for K and  $\epsilon$ . The 3D simulations require approximately 8.5 CPU minutes per iteration, or 3.5 CPUhours for a converged solution on a CRAY-2 with 35.1 MW of memory needed. Alternatively, 4.5 CPUhours per iteration, or 4.7 CPUdays for a converged solution is required on an SGI IRIS 4D/25G with 64 MByte RAM. Time requirements for various computers are summarized in Table 2.

### **3.5 Mesh Refinement**

Since a mesh refinement analysis using 3-D simulations is computationally expensive, several 2-D simulations of the SEN were performed to determine the optimal number of nodes and elements needed to produce accurate results in a reasonable CPU time.<sup>29</sup> The 2-D simulation consists of a section through the central (x-z) plane of the outlet ports (Figure 2). Finite-element meshes consisting of 484, 1073, 1848 and 4197 nodes were tested. The two finest meshes (1848 and 4197 nodes) produce almost the same jet characteristics at the nozzle outlet plane. Coarser meshes converge much faster but produce increasing differences in the results. For example, the maximum deviation in size of the recirculation zone reached -10% for the 484-node mesh. Differences in jet speed predicted across the outlet port were smaller, as compared in Figure 4. Since the finest 4197-node mesh requires over 3 times as much computation as the 1848-node mesh, (225 versus 71 CPU seconds per iteration on an SGI IRIS4D/35G), the 1848-node mesh was adopted as the optimum compromise. The 3-D mesh was constructed to approximate the refinement of this mesh.

## **4. 3-D SEN MODEL RESULTS**

The flow field calculated using the standard conditions in Table 1 is depicted in Figure 5. A comparison with Figure 6 shows the effect of changing the angle of the ports from 15° down (with respect to the horizontal) to 15° up. The flow pattern, jet speed, and turbulence intensity are similar for the two SEN configurations. In both cases, the fluid momentum makes the jet exit from the port at a steeper downward angle than that of the port edges. The average jet angle,  $\theta_{zx}$ , is defined using a weighted average with the mass flow rate:

$$\theta_{zx} = \tan^{-1} \left( \frac{\sum_{i=1}^{NE} (\overline{v_z})_i (\overline{V})_i (\Delta_x)_i (\Delta_z)_i}{\sum_{i=1}^{NE} (\overline{v_x})_i (\overline{V})_i (\Delta_x)_i (\Delta_z)_i} \right) \quad (21)$$

where NE is the number of elements in the plane of the port outlet where fluid exits from the port,  $\Delta x$  and  $\Delta z$  are the lengths of the element sizes in the x and z directions, respectively,  $(\overline{V})_i$  is the nodal speed, and  $(\overline{v_x})_i$  and  $(\overline{v_z})_i$  are the nodal velocity components in the x and z directions, respectively. The mean jet angle is calculated as  $24^\circ$  down and  $10^\circ$  down for the SEN with  $15^\circ$  downward and  $15^\circ$  upward angled ports, respectively.

Flow exits mainly from the lower half of the port, with a recirculation zone found in the upper portion as seen in Figures 5 and 6. The main jet exiting from the SEN is almost parallel to the port side walls. This is indicated by calculating the average spread angle in the x-y plane. This angle is defined as:

$$\theta_{yx} = \tan^{-1} \left( \frac{\sum_{i=1}^{NE} (\overline{v_y})_i (\overline{V})_i (\Delta_x)_i (\Delta_y)_i}{\sum_{i=1}^{NE} (\overline{v_x})_i (\overline{V})_i (\Delta_x)_i (\Delta_y)_i} \right) \quad (22)$$

The average spread angle is found to be less than  $1^\circ$  for both SEN configurations. Hence, the flow is predominantly two-dimensional as it exits the nozzle ports. However, a slight vortex induces the jet to spread significantly in the y direction at the lower outside corner of the port, where the spread angle increases locally to  $15^\circ$  for both ports studied.

Figure 7 shows cross-sections through the nozzle looking into the left port. The vortex is seen more clearly in these cross-sections. The vortex is stronger in the  $15^\circ$  upward angled SEN pictured in this figure, than in the  $15^\circ$  down SEN, and it persists through the entire bottom of the SEN. Naturally, the imposed symmetry of this model implies that four symmetrical vortices are present in the whole SEN. The swirling motion of each vortex induces the flow to lift slightly upwards against the sides of the port. This results in a smaller stagnant recirculation zone at the sides of the upper part of the port than at the center, as seen in Figure 6.

## 5. COMPARISON WITH EXPERIMENTS

Observations and measurements were made using full-scale water models of the tundish, SEN, and mold region of the caster located at Armco Steel in Middletown, Ohio and at Inland Steel in East Chicago, Indiana. Process conditions, including casting speed and SEN geometry, were similar to the numerical simulations.

### 5.1 Observations

Figure 8 shows a typical flow pattern seen in a front view ( $x$ - $z$  plane) of a SEN with  $15^\circ$  upward angled ports. A small amount of air (3%) was injected to help visualize the flow pattern in this photo. The 3-D simulations appear very similar to the observed flow pattern. As seen in the snapshot, Figure 8, the jet is directed approximately  $12^\circ$  down, which is close to the predicted value of  $10^\circ$  down. Note that the fluid momentum always makes the jet exit at a steeper downward angle than that of the port edge. A relatively low velocity recirculation region was observed in the upper portion of the port. This is associated with the “oversized” nature of the ports used in this type of SEN, as the combined area of the two port exits significantly exceeds the bore area. This behavior is roughly consistent with previous findings.<sup>15, 17</sup> Careful observation of the recirculation zone shows that the flow is not completely uniform across the port. Instead, it exits slightly higher up the sides than the center, which is also captured in the numerical simulations. However, in the experimental observations of the water model, the shape of the recirculation zone changes greatly with time.

Figure 9 shows schematics of the common flow patterns observed in a side view ( $y$ - $z$  plane) of a  $15^\circ$  down SEN at the plane of the port exit. These sketches are based on videos taken by Schmidt and Byrne,<sup>30</sup> looking directly into the port. Their SEN geometry was similar to that of the present work, except that the ports are larger (70 x 100 mm) and more oversized. A swirling action clearly exists inside the SEN port. As shown in Figure 9 (b), the swirling sometimes consists of two symmetrical vortexes. This flow pattern corroborates the model predictions discussed earlier. Vortical structures occupying a large portion of the port, as sketched in Figures 9 (c) and (d), are more frequently observed.

According to the observations of Schmidt and Byrne,<sup>30</sup> the vortex size and rotational direction evolve through time, “flipping” through the various modes shown in Figures 9 (c), (b) and (d). The most stable vortex mode was affected by the flow conditions at the SEN inlet. The clockwise vortex, sketched in Figure 9 (d), is more likely when the slide gate, and hence the tube, is completely open. The counter-clockwise vortex, Figure 9 (c), dominates when the fraction of the

tube blocked by the slide gate exceeds a critical value. Counter-clockwise rotation is consistent with the direction of the asymmetrical flow through the SEN induced by the slide gate. A critical position of the slide gate results in rapid flipping between flow patterns within a period of about 1 - 5 s. Quality problems due to severe surface turbulence were observed in the steel caster at a critical flow rate (or casting speed), which might correspond to the critical slide gate opening position.<sup>30</sup> Stronger vortexes have been observed with thicker walled SENs.<sup>30</sup>

The flow behavior observed in the water models of the present work was qualitatively similar to Schmidt and Byrne's experiments, but the strength of the vortexes was weaker and no dramatic changes at critical speeds or slide gate positions were observed. More swirling and turbulence were observed with the 15° up SEN as compared with the 15° down. The axis of rotation of the vortex was roughly horizontal, regardless of port angle.

## ***5.2 Velocity Measurements***

Velocity measurements near the SEN outlet port were taken with a single hot-wire anemometer probe. The hot-wire probe was oriented perpendicular to the principal flow direction, so meaningful results could be obtained with a single probe. Figure 10 shows a portion of a typical, unfiltered signal, recorded on a strip chart. This chart does not show the full range of velocities encountered, since all values exceeding 1.5 m/s were truncated to 1.5 m/s. The signal is proportional to heat transfer, and hence the probe always registers a positive value, regardless of the direction of the flow. Thus, only speed could be measured using this probe.

Large fluctuations are present in the speed signal near the SEN outlet port as shown in Figure 10, and emphasize the unsteady nature of the flow as discussed in the experimental observations. Fluctuations were particularly evident in the middle and upper regions of the port, where flow reversals were often observed. There appears to be at least two time scales for the fluctuations. A high-frequency mode, of more than  $10\text{s}^{-1}$ , is likely caused by the variation of the small-scale turbulent structure. Superimposed on these high-frequency fluctuations is a low-frequency mode ranging from  $0.25\text{s}^{-1}$  to  $1\text{s}^{-1}$  which was often recorded in the central and upper portions of the port. This low-frequency mode may coincide with observed macroscopic changes in the flow pattern and large-scale turbulent eddies exiting the nozzle similar to the ones depicted in Figure 9.

Figure 11 plots the time-averaged speed measurements across the outlet plane of the SEN ports. Each experimental average speed,  $\overline{V}_{\text{measured}}$ , was deduced from analysis of the probe signal,  $V_{\text{signal}}$ , over an extended period of time,  $T$ ,

$$\overline{V}_{\text{measured}} = \frac{1}{T} \int_0^T V_{\text{signal}} dt \quad (23)$$

using both a multimeter needle and the strip chart recorder. Observations of the needle movement were aided by electronically damping the signal to produce a partially time-averaged signal. The “error” bars on the data points of  $\overline{V}_{\text{measured}}$  in Figure 11 indicate the uncertainties in both probe location and speed measurements. Based on combined observations of the strip chart and needle, the speed “error” bars are estimated to contain about 67% of the instantaneous data (one standard deviation).

The highest uncertainty in the measurements was in the upper region of the ports where the instantaneous x-component of velocity changed directions drastically from positive (out of the port) to negative (into the port). This flow reversal could not be captured by the hot-wire probe used in these experiments since it only provided measurements of the velocity magnitude. Because all velocities were recorded as positive, larger time-averaged speeds were measured in the upper regions of the port, as shown in Figure 11.

To best compare the mean speed signal determined in the experiments with the various velocity components computed by the mathematical model, the following inequality must be invoked:

$$\overline{V}_{\text{measured}} \leq \overline{V}_{\text{max}} = \sqrt{\frac{1}{T} \int_0^T V_{\text{signal}}^2 dt} \quad (24)$$

where the largest measured speed signal is given by:

$$V_{\text{signal}} = \sqrt{(\overline{v_x} + v_x')^2 + (\overline{v_y} + v_y')^2 + (\overline{v_z} + v_z')^2} \quad (25)$$

Expanding the terms of equation (25) and averaging using equation (24) leads to the following expression.

$$\overline{V}_{\max} = \sqrt{\overline{v_x^2} + \overline{v_y^2} + \overline{v_z^2} + \overline{v_x'^2} + \overline{v_y'^2} + \overline{v_z'^2}} \quad (26)$$

The mathematical model accounts for velocity fluctuations through the turbulent kinetic energy as follows.

$$K = \frac{1}{2} \left( \overline{v_x'^2} + \overline{v_y'^2} + \overline{v_z'^2} \right) \quad (27)$$

Assuming isotropic turbulence, the upper bound on the measured speed signal from equations (26) and (27) becomes:

$$\overline{V}_{\max} = \sqrt{\overline{v_x^2} + \overline{v_y^2} + \overline{v_z^2} + 2K} \quad (28)$$

Figure 11 shows the measured speed,  $\overline{V}_{\text{measured}}$ , and computed average speed,  $\overline{V}_{\max}$ , at the SEN outlet plane. The components that make up the computed speed signal,  $\sqrt{\overline{v_x^2} + \overline{v_y^2} + \overline{v_z^2}}$ , and  $\sqrt{2K}$  are also included in Figure 11. The model predictions of the average speed agree satisfactorily in the lower portion of the SEN port.

Although within experimental uncertainty, the 3-D simulations underpredict the speeds in the low-velocity, upper region of the port. This might be due to underprediction of the turbulent velocity fluctuations calculated by the K- $\epsilon$  model, which are seen in Figure 11 to be more important in this region. Alternatively, this could be caused by the inability of the steady-state simulation to capture unsteady flow features, such as the low frequency fluctuation between flow patterns shown in Figure 9. Another possibility is the effect of flow in the mold, investigated in section 7.

## 6. COMPARISON WITH 2-D SEN MODEL

Since the average spread angle computed from the 3-D simulations was about  $1^\circ$  (see section 4), the spatial-mean flow field is mainly confined to the 2-D horizontal (x-z) plane. It is to be noted, however, that the flow at the outlet of the port is locally three-dimensional with a pair of clockwise rotating vortices as discussed in the previous section. Since the SEN outlet ports are square and have almost the same width (60 mm) as the SEN bore diameter (76 mm), it was surmised that the major characteristics of the flow pattern could be captured with a 2-D simulation of the SEN using a slice in the x-z plane made through the center-plane of the ports. Previous experimental and numerical works<sup>15</sup> confirm this. For the 2-D simulations, the SEN nozzle bore,

port height, thickness, angle and well depth are given in Table 1; the SEN tube was extended to its full working length of 501 mm. Both ports are included in the numerical simulation, thus allowing investigation of asymmetrical flow through the SEN in future work. Boundary conditions are applied along the edges of the 2-D domain as discussed in section 3. The mesh for the 2-D simulations consists of 1848 nodes, 1740 four-node, linear, quadrilateral elements and 154 four-node near-wall elements. This achieves a similar degree of mesh refinement as used in the 3-D SEN mesh.

The 2-D assumption removes the  $y$ -component and its derivatives from the governing equations, equations (1-5), thus reducing the number of unknown variables and equations by one. In addition, the size of the mesh is greatly reduced. Together, this decreases the computation time needed to run a simulation by almost two orders of magnitude. Table 2 compares the CPU time required per iteration for the full 2-D mesh and the one-quarter 3-D mesh on various computers. Since the same convergence strategy and number of iterations are needed for the 2-D and 3-D simulations, these CPU time values also indicate the relative cost of a complete simulation. The 2-D model runs between 35 and 88 times faster than the 3-D model. The speed differential on the workstation is greater because internal memory limitations induce excessive virtual-memory swapping of the large files involved with the 3-D model. For example, the time needed for a simulation reduces from four days (3-D model) to one hour (2-D model) on an IRIS 4D/25G. Using a coarser mesh would also speed up the calculations, but the results become less reliable. Table 2 shows that the CRAY-2 supercomputer runs about 5 - 10 times faster than the workstations, if memory limitations are not a factor.

The 3-D, 90 x 60 mm, SEN simulations were compared with the 2-D results for a 90 mm SEN to validate the 2-D assumption. The calculated velocity vectors at the SEN centerplane for both 2-D and 3-D models are displayed in Figure 12 for the 15° downward angled ports. Table 3 summarizes the average exit jet characteristics as determined by the 2-D and 3-D simulations. The 2-D simulation reproduces the jet angle, but slightly underpredicts the average jet speed, turbulence intensity and size of the recirculation zone. Similar agreement was observed with the 15° upward angled ports.

The speed distributions along several vertical lines through the plane of the outlet port are plotted in Figure 13 for the 3-D and 2-D simulations. Near the outer edge of the port, the velocity is slower and the flow extends slightly further up the wall due to the presence of the vortex (see Figure 7), as discussed previously. The speed profile obtained by the 2-D simulation compares surprisingly well with the 3-D profiles at the centerline and quarterline. The 2-D results also

reasonably approximate the 3-D speed profile averaged across the y direction. At the bottom edge of the port, however, the 3-D simulation predicts a slight increase in velocity, while the 2-D simulation predicts a gradual decline.

Figure 14 compares the average turbulent kinetic energy profiles for the 3-D and 2-D simulations. The turbulent kinetic energy reaches peak values at the bottom wall of the port and about half-way up the port. This second, smaller peak corresponds to the strong shear layer at the boundary between the jet and the recirculation region. The 2-D simulation is seen to overpredict the turbulent kinetic energy at the nozzle bottom port, and underpredict it in the shear zone as compared to the centerline of the 3-D simulation. This could be related to the three-dimensionality of the flow in these regions. Similar trends and comparisons are observed for the turbulent dissipation,  $\epsilon$ .

Overall, the 2-D simulations satisfactorily capture the flow pattern through the bifurcated SEN and reasonably predict the jet characteristics. Since 3-D simulations of the SEN flow are currently only feasible on supercomputers, the tremendous reduction in computational expenses and resources, offered by the 2-D simulations, enables investigation of the effects of design parameters such as nozzle bore, port height and thickness, casting speed, and slide gate positions. However, the 2-D approach has drawbacks, such as the inability to capture the vortex formation inside the port or to study the effect of port geometry and width.

## **7. COMBINED SEN AND MOLD MODEL**

The work presented thus far has focused on modeling the SEN by itself and assumes that changes in the downstream conditions beyond the SEN port outlet have negligible effect on the exit jet. These conditions include mold operating variables, such as SEN submergence depth and mold width, as well as numerical issues such as the zero stress boundary condition along the port outlet. In previous studies<sup>17, 15, 2</sup> simulations of the SEN provided appropriate inlet boundary conditions for modeling flow in the mold. To investigate the validity of analyzing the SEN and mold regions separately, a two-dimensional finite-element model combining the SEN and the mold was created.

The mesh used to simulate the flow in both the SEN and mold consists of 4079 four-node, quadrilateral elements and 162 near-wall elements. It was constructed by attaching 3339 elements of half of the mold to 902 elements of half of the 15° down SEN used in the 2-D SEN simulations. The geometrical configuration and resulting flow patterns under standard conditions, given in Table 1, are shown in Figure 15. In this simulation, symmetry down the center of the mold (x-z plane) is

assumed. Near-wall elements are applied along the left boundary of the mold and zero-normal gradients are imposed at the bottom boundary of the computational domain.

This model was more prone to numerical instabilities than separate models of the SEN and mold. When solving the velocity field with a turbulence model from a zero initial condition, the solution diverges even with a small relaxation factor. To overcome this stability problem, a velocity field is first calculated without activating the turbulence model. The partially converged laminar solution that results is then used as an initial guess for calculating the final flow field. This method significantly improves the stability of the solution because the turbulent phase of the calculation needs to solve for only the kinetic energy and dissipation distributions, along with minor adjustments to the velocity fields corresponding to the turbulent nature of the flow. The computational cost was 894 CPUs for each of 20 iterations with turbulence on the IRIS 4D/25G after the converged laminar solution was achieved.

The results of the combined model are generally very similar to the separate models in both the SEN and mold regions. Flow in the mold reproduces the familiar downward jet flanked by upper and lower recirculation zones, and is similar to previous results.<sup>15</sup> Table 3 contains the average jet characteristics for the SEN region of the combined model under standard operating conditions. The differences between the jet characteristics of the combined model and the separate 2-D and 3-D models of the SEN alone are relatively small. For example, the speed profiles along the outlet plane of the port are very similar. The flow pattern produced in the recirculation zone just inside the port is markedly different, however. The velocities entering the top half of the port in the separate SEN models are parallel to the top edge. The combined model predicts a more complex pattern in this region, caused by flow moving downward along the outside of the SEN. This alters the shape of recirculation zone near the upper port outlet, producing a stagnation point on the top edge of the port (see Figure 16b).

This slow moving region is important in the continuous casting process because stagnation points are believed to be prime locations for alumina inclusions to attach to the SEN walls and build up, possibly clogging the SEN.<sup>8</sup> Figure 16 also shows fluid being carried down from the slag layer at the top surface and entering into the nozzle port. Other researchers have used combined SEN and mold models without reporting this effect.<sup>31, 32</sup> However, these models have used meshes much more coarse than the one used in the present study, and a fine mesh is required to capture this phenomenon.

## **7.1 Submergence Depth**

Close-up views of the results of the combined model are given in Figure 16 for different submergence depths. Differences from the separate model of the SEN are slightly more pronounced in the low velocity region with the greater (203 mm) submergence depth. This is probably due to the higher velocities down the outside wall of the SEN directly above the outlet port in this case. The shape of the recirculation zone in the upper region of the port of the shallow (51 mm) submerged SEN, shown in Figure 15a is only slightly different from that in Figure 12, which was calculated with a zero gradient outlet boundary condition.

The results in Table 3 show that the characteristics of the jet leaving the lower portion of the nozzle port do not vary significantly with submergence depth. Furthermore, the results are similar to the those calculated using the separate model of the SEN. Thus, it appears that the downstream flow conditions do not significantly affect the jet exiting this portion of the SEN. Because flow in the mold is governed mainly by the characteristics of the high-velocity jet leaving the lower portion of the nozzle port, the effect of increasing the submergence depth from 51 mm to 203 mm on flow entering the mold is small.

This finding is consistent with the experimental observation that the flow pattern is relatively insensitive to submergence depth. The flow in the continuous casting process is driven by gravity and hence a pressure difference between the tundish and mold. Changing the SEN submergence depth only changes the total pressure at the SEN port outlet, not the pressure difference between the top and bottom of the SEN port. If the difference in levels between the liquid surfaces in the mold and tundish are maintained, then there should be no difference in pressure gradients along the SEN outlet. If there is a level difference, then the flow rate will change, or the flow control devices must be adjusted. These have a significant effect on the flow pattern that is more important than the subtle differences discussed here.

## **8. CONCLUSIONS**

The three-dimensional finite-element model described in this work is reasonably able to reproduce the qualitative, time-averaged behavior of turbulent flow in a bifurcated submerged-entry-nozzle. Flow through the SEN is characterized by a strongly fluctuating, swirling jet leaving the bottom half of the two ports with a relatively low-velocity recirculation zone found near the top of the ports. The predictions also show reasonable quantitative agreement with measurements in the high velocity region of the jet exiting the lower portion of the nozzle.

The time-average speed is slightly under-predicted in the low velocity regions of the SEN port, even when turbulent velocity fluctuations are accounted for through the turbulent kinetic energy,  $K$ , determined from the  $K$ - $\epsilon$  model. This is attributed in part to the inability of the steady-state flow model to predict the low-frequency, time-dependent fluctuations between flow patterns, which were observed experimentally. Flow in the low-velocity regions is also affected greatly by flow in the mold cavity, as demonstrated with a combined model of the nozzle and mold.

The results of this work suggest that a separate numerical model of the nozzle should provide reasonable inlet boundary conditions for subsequent predictions of the time-averaged flow pattern developed in the mold, which is governed mainly by the characteristics of the high-velocity jet leaving the nozzle. It appears reasonable to divide the nozzle and its outlet domain in order to save computation resources. This is important for preliminary parametric studies to aid in SEN design. In addition, a 2-D model can be used with caution to economically gain insights into the flow pattern and jet characteristics in the plane of the 2-D model. Vortexing and other subtle aspects of the flow can only be captured with the 3-D model, but almost two orders of magnitude more computation is required.

The results of this work also suggest that the steady-state  $K$ - $\epsilon$  model of turbulent flow in the separated nozzle, even in 3-D, is deficient in quantifying the velocities in regions where time-dependent variations in the flow pattern are significant. Time-dependent variations in flow leaving the nozzle may be important to transient changes in the flow pattern observed in the mold, which may create surface turbulence and associated quality problems. To study these phenomena, water model experiments and plant testing are still needed.

## **ACKNOWLEDGMENTS**

The authors wish to thank the steel companies: Armco Inc. (Middletown, OH), Inland Steel Corp. (East Chicago, IN), LTV Steel (Cleveland, OH) and BHP Co. Ltd. (Wallsend, Australia) and the National Science Foundation (DDM-8957195) for grants which made this research possible. We are also indebted to researchers at Armco and Inland for providing their water modeling facilities and technical support and at Bethlehem Steel for sharing results. Thanks also go to Fluid Dynamics Inc., (Evanston, IL) for providing FIDAP and to the National Center for Supercomputing Applications (Urbana, Illinois) for time on the CRAY-2.

## LIST OF FIGURES

- Figure 1. Schematic of the continuous casting process showing tundish, SEN and mold
- Figure 2. Schematic of typical SEN used in steel slab casting
- Figure 3. Mesh and boundary conditions used in 3-D SEN model simulations
- Figure 4. Effect of mesh density on x-velocity down nozzle outlet port (2-D simulation)
- Figure 5. Calculated velocities in bottom portion of a 15° down SEN
- Figure 6. Calculated velocities in bottom portion of a 15° up SEN
- Figure 7. Calculated velocities in longitudinal sections through bottom of 15° up SEN.
- Figure 8. Flow pattern in water model using 15° up SEN
- Figure 9. Typical flow patterns observed in port of SEN water model.<sup>30</sup>
- Figure 10. Recorded speed - time signal (100 mm from port outlet and 78 mm below top of port.)
- Figure 11. Comparison of experimental and predicted speed down centerline of SEN port exit (x-z plane)
- Figure 12. Calculated velocity fields at center plane of 15° down port  
a) 3-D SEN model            b) 2-D SEN model
- Figure 13. Comparison of jet speed down outlet port exit for 2-D and 3-D SEN simulations
- Figure 14. Comparison of turbulent kinetic energy down outlet port exit for 2-D and 3-D SEN simulations
- Figure 15. Calculated velocities in combined SEN / mold model (51 mm submergence depth)
- Figure 16. Calculated velocities near SEN port in combined SEN / mold model  
a) 51-mm submergence depth    b) 203-mm submergence depth

**Table 1 Standard simulation conditions**

Nozzle Dimensions:	
bore diameter	76.0 mm
length - total	501.2 mm
modeled	300.0 mm
port angle	15° down
port height	90.0 mm
port thickness	25.5 mm
port width	60.0 mm
recessed bottom depth	13.0 mm
Mold Dimensions:	
width	1.32 m
thickness	0.22 m
Molecular Viscosity, $\mu_0$	0.056 kg m <sup>-1</sup> s <sup>-1</sup>
Density, $\rho$	7021 kg m <sup>-3</sup>
Casting Speed	0.01563 m s <sup>-1</sup>
Solution Procedure:	
strategy	25 Suc. Sub. Iterations
relaxation factor	0.25
streamwise upwinding factor	1.0
pressure penalty function	
parameter, $\sigma$	10 <sup>-8</sup>
Inlet Conditions:	
x-velocity, $v_x$	0.0 m s <sup>-1</sup>
y-velocity, $v_y$	0.0 m s <sup>-1</sup>
z-velocity, $v_z$	-1.0 m s <sup>-1</sup>
turbulent kinetic energy, K	0.00425 m <sup>2</sup> s <sup>-2</sup>
dissipation, $\epsilon$	0.025 m <sup>2</sup> s <sup>-3</sup>
Initial Guess	
velocity	0.0 m s <sup>-1</sup>
turbulent kinetic energy	0.0035 m <sup>2</sup> s <sup>-2</sup>
dissipation	0.020 m <sup>2</sup> s <sup>-3</sup>
Inlet Reynolds Number	95,400

*Table 2 Computer Time Requirements*

Computer	Time Per Iteration (CPU sec)	
	2-D Model 1848 Nodes	3-D Model 5415 Nodes
CRAY - 2	14.3	499.4
IRIS 4D/35G	45.0 †	—
IBM RISC 6000	58.6	—
IRIS 4D/25G	142.5	12,600

† estimated

**Table 3 Average Jet Characteristics at Nozzle Exit**  
*(Standard Conditions Table 1)*

	3-D Model	2-D Model	Combined Model (51 mm Submergence)	Combined Model (203 mm Submergence)
Jet Speed (m/s)	0.94	0.97	0.87	0.90
Jet Angle (°) (below horizontal)	24	24	23	22
Turbulence Intensity (%)	15	12	13	15
Recirculation Zone (% of outlet area)	42	38	32	35

## REFERENCES

1. International Iron and Steel Institute, 'Percentage of Crude Steel Continuously Cast, 1981-1990', **18** (13), 16 (1991).
2. X. Huang, B.G. Thomas and F.M. Najjar, 'Modeling Superheat Removal during Continuous Casting of Steel Slabs', *Metallurgical Transactions B*, (in print), (1992).
3. H. Nakato, M. Ozawa, K. Kinoshita, Y. Habu and T. Emi, 'Factors Affecting the Formation of Shell and Longitudinal Cracks in Mold during High Speed Continuous Casting of Slabs', *Trans. Iron Steel Inst. Japan*, **24** (11), 957-965 (1984).
4. J. Herbertson, Q.L. He, P.J. Flint and R.B. Mahapatra, 'Modelling of Metal Delivery to Continuous Casting Moulds', *74th Steelmaking Conference*, Washington, D.C., 1991, **74**, pp. 171-185, Iron and Steel Society, Inc., Warrendale, PA.
5. N.T. Mills and L.F. Barnhardt, 'The development of submerged entry tundish nozzles', *Journal of Metals*, (November), 37-43 (1971).
6. R. Sobolewski and D.J. Hurtuk, 'Water Modeling of Slab Caster Flow Conditions', *Proc. Second Process Technology Conf.*, 1982, **2**, pp. 160-165, Iron and Steel Society, Inc., Warrendale, PA.
7. A. Ferretti, M. Podrini and G. Di Schino, 'Submerged nozzle optimization to improve stainless steel surface quality at Treni Steelworks', *68th Steelmaking Conference*, 1985, **68**, Iron and Steel Society, Inc., Warrendale, PA.
8. S. Dawson, 'Tundish Nozzle Blockage During the Continuous Casting of Aluminum-killed Steel', *73rd Steelmaking Conference*, Detroit, MI, 1990, **73**, pp. 15-31, Iron and Steel Society, Inc., Warrendale, PA.
9. N.A. McPherson, S.J. Lee, G.J. Roberts and J. Purdie, 'Continuous casting refractories for improved operating and quality performance', **17** (1), 43-45 (1990).

10. R.C. Sussman, M. Burns, X. Huang and B.G. Thomas, 'Inclusion Particle Behavior in a Continuous Slab Casting Mold', *10th Process Technology Conference*, Toronto, Canada, 1992, **75**, , Iron and Steel Society, Inc., Warrendale, PA.
11. K. Takantani, K. Nakai, N. Kasai, T. Watanabe and H. Nakajima, 'Analysis of heat transfer and fluid flow in the continuous casting mold with electronic brake', *6th International Iron and Steel Congress*, Nagoya, Japan, 1990, **4**, pp. 430-437, Iron and Steel Institute of Japan, Tokyo, Japan.
12. H. Tozawa, H. Kitaoka, K. Sorimachi, H. Ishizuka and M. Ohnishi, 'Flow control of molten steel in continuous casting mold', *6th International Iron and Steel Congress*, Nagoya, Japan, 1990, **4**, pp. 438-445, Iron and Steel Institute of Japan, Tokyo, Japan.
13. A. Preuer, Voest Alpine, Linz, Austria, private communication, 1992.
14. Y.H. Wang, '3-D Mathematical Model Simulation on the Tundish Gate and Its Effect in the Continuous Casting Mold', *10th Process Technology Conference*, Toronto, Ontario, Canada, 1992, **75**, , Iron and Steel Society, Inc., Warrendale, PA.
15. B.G. Thomas, L.M. Mika and F.M. Najjar, 'Simulation of Fluid Flow Inside a Continuous Slab Casting Machine', *Metallurgical Transactions B*, **21B** (2, April), 387-400 (1990).
16. B.G. Thomas and F.M. Najjar, 'Finite-Element Modeling of Turbulent Fluid Flow and Heat Transfer in Continuous Casting', *Applied Mathematical Modelling*, **15** (May), 226-243 (1991).
17. F.M. Najjar, D.E. Hershey and B.G. Thomas, 'Turbulent Flow of Steel Through Submerged Bifurcated Nozzles into Continuous Casting Molds', *Fourth FIDAP Users Conference*, Evanston, IL, 1991, pp. 1-55, Fluid Dynamics International, Inc., 500 Davis Ave., Suite 400, Evanston, IL.
18. F.M. Najjar, 'Finite-Element Modelling Of Turbulent Fluid Flow and Heat Transfer Through Bifurcated Nozzles In Continuous Steel Slab Casters', M.S. Thesis, University of Illinois, 1990.
19. Y.H. Wang and D.E. Hershey, *Unpublished research*. 1991.

20. M. Yao, 'Flow Simulation of Molten Steel for Immersion Nozzle Design in Continuous Casting Process', *Modeling and Control of Casting and Welding Processes IV*, 1988, pp. 893-898, TMS / AIME, Warrendale, PA.
21. M.S. Engleman, 'FIDAP Theoretical Manual - Revision 6.0', *Report*, Fluid Dynamics International, Inc., 1991.
22. J.L. Sohn, 'Evaluation of FIDAP on some classical laminar and turbulent benchmarks', *International Journal for Numerical Methods in Fluids*, **8**, 1469-1490 (1988).
23. B.E. Launder and D.B. Spalding, 'Numerical Computation of Turbulent Flows', *Computer Methods in Applied Mechanics and Engr*, **13**, 269-289 (1974).
24. B.E. Launder and D.B. Spalding, *Mathematical Models of Turbulence*, London Academic Press, 1972.
25. W. Rodi, 'Turbulence Models and Their Application in Hydraulics - A State of the Art Review', *Report*, University of Karlsruhe, Karlsruhe, Germany, 1980.
26. V. Haroutunian and M.S. Engelman, 'On Modeling Wall-Bound Turbulent Flows Using Specialized Near-Wall Finite Elements and the Standard K- $\epsilon$  Turbulence Model', *Report*, Fluid Dynamics International, 1989.
27. H. Schlichting, *Boundary-Layer Theory*, McGraw Hill, 1955.
28. J. Nikuradse, 'Gesetzmaßigkeit der Turbulenenten Stromung in Glatten Rohren', *Forschg. Arb. Ing. Wed.*, **356**, (1932).
29. D.E. Hershey, 'Turbulent Flow of Molten Steel through Submerged Bifurcated Nozzles in the Continuous Casting Process', M.S. Thesis, University of Illinois, 1992.
30. M. Schmidt and M. Byrne, Bethlehem Steel, Sparrows Point, Baltimore, private communication, 1992.

31. M. Yao, M. Ichimiya, S. Syozo, K. Suzuki, K. Sugiyama and R. Mesaki, 'Three Dimensional Analysis of Molten Metal Flow in Continuous Casting Mould', *68th Steelmaking Conference*, Detroit, MI, 1985, **68**, pp. 27-33, Iron and Steel Society, Inc., Warrendale, PA.
32. P.J. Flint, 'A three-dimensional finite difference model of heat transfer, fluid flow and solidification in the continuous slab caster', *73rd Steelmaking Conference*, Detroit, MI, 1990, **73**, pp. 481-490, Iron and Steel Society, Inc., Warrendale, PA.

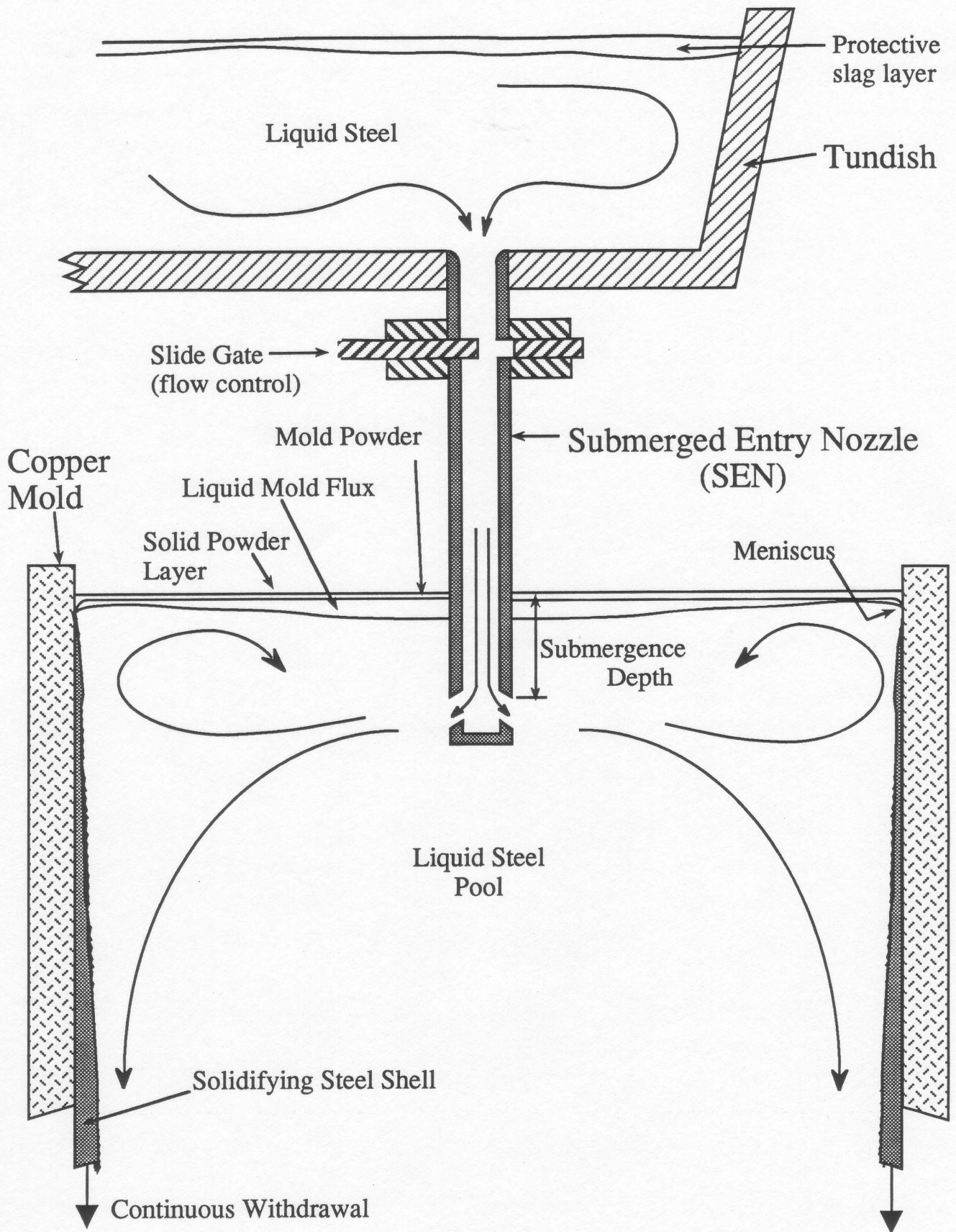


Figure 1. Schematic of the continuous casting process showing tundish, SEN and mold

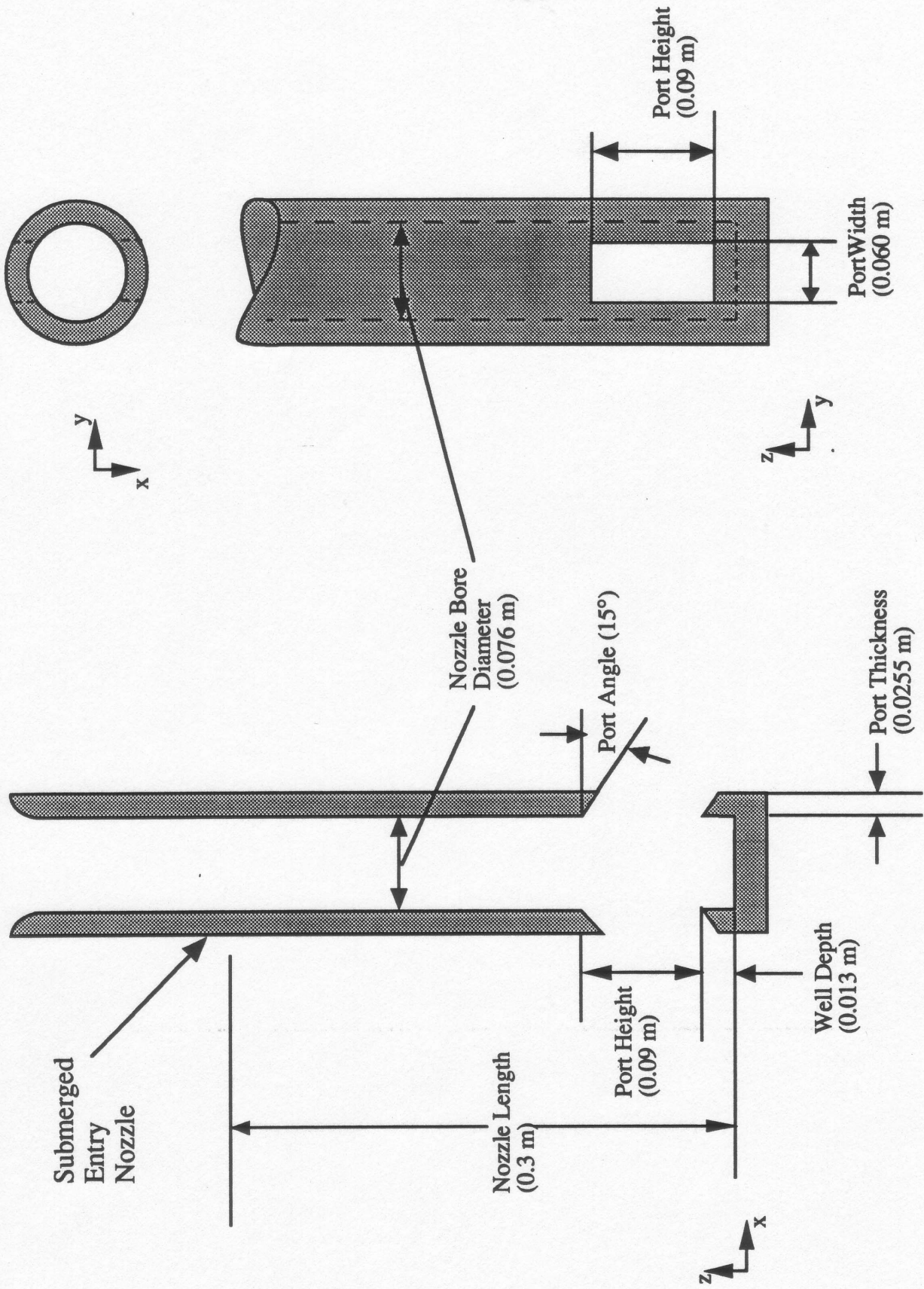


Figure 2. Schematic of typical SEN used in steel slab casting

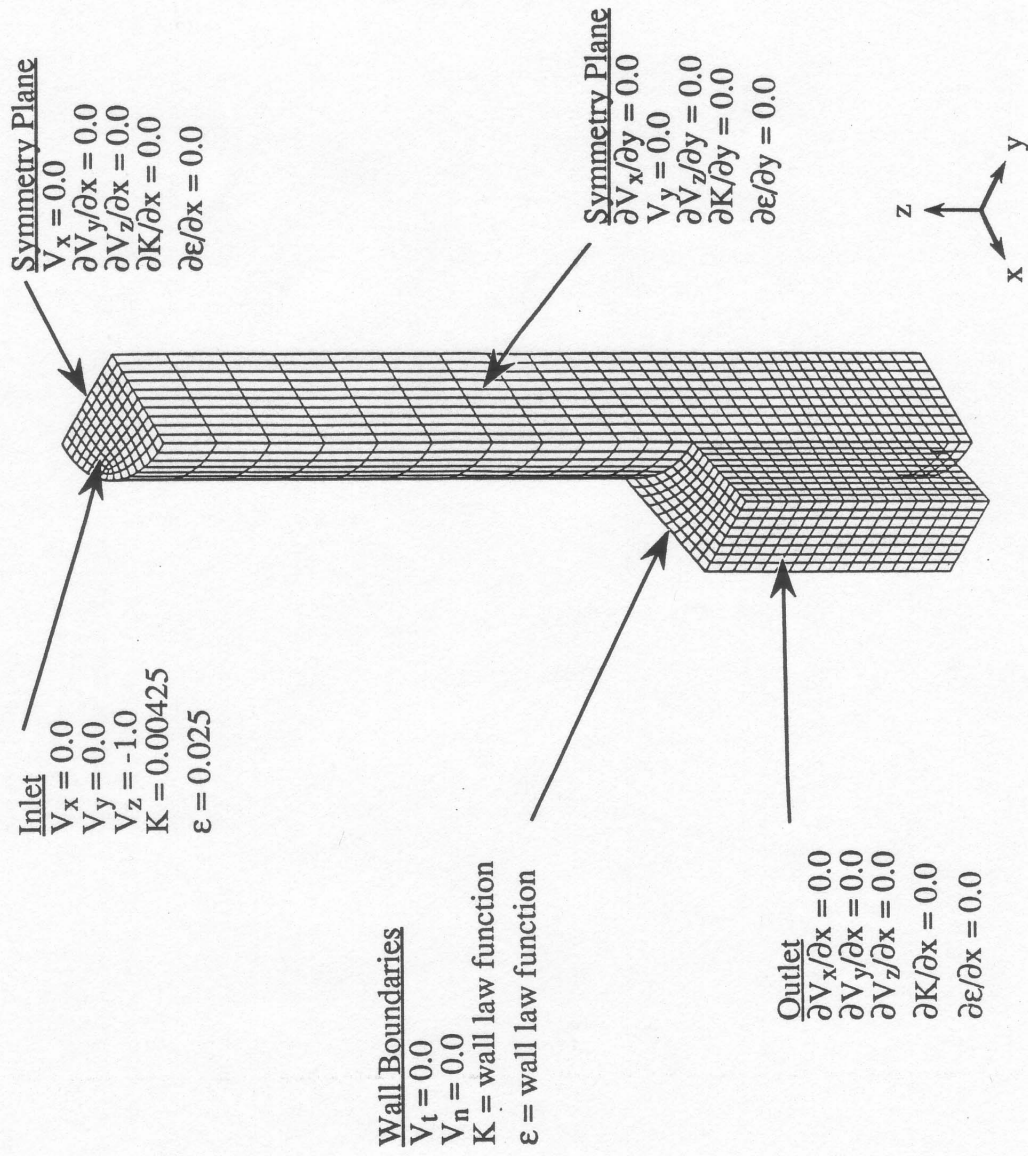


Figure 3. Mesh and boundary conditions used in 3-D SEN model simulations

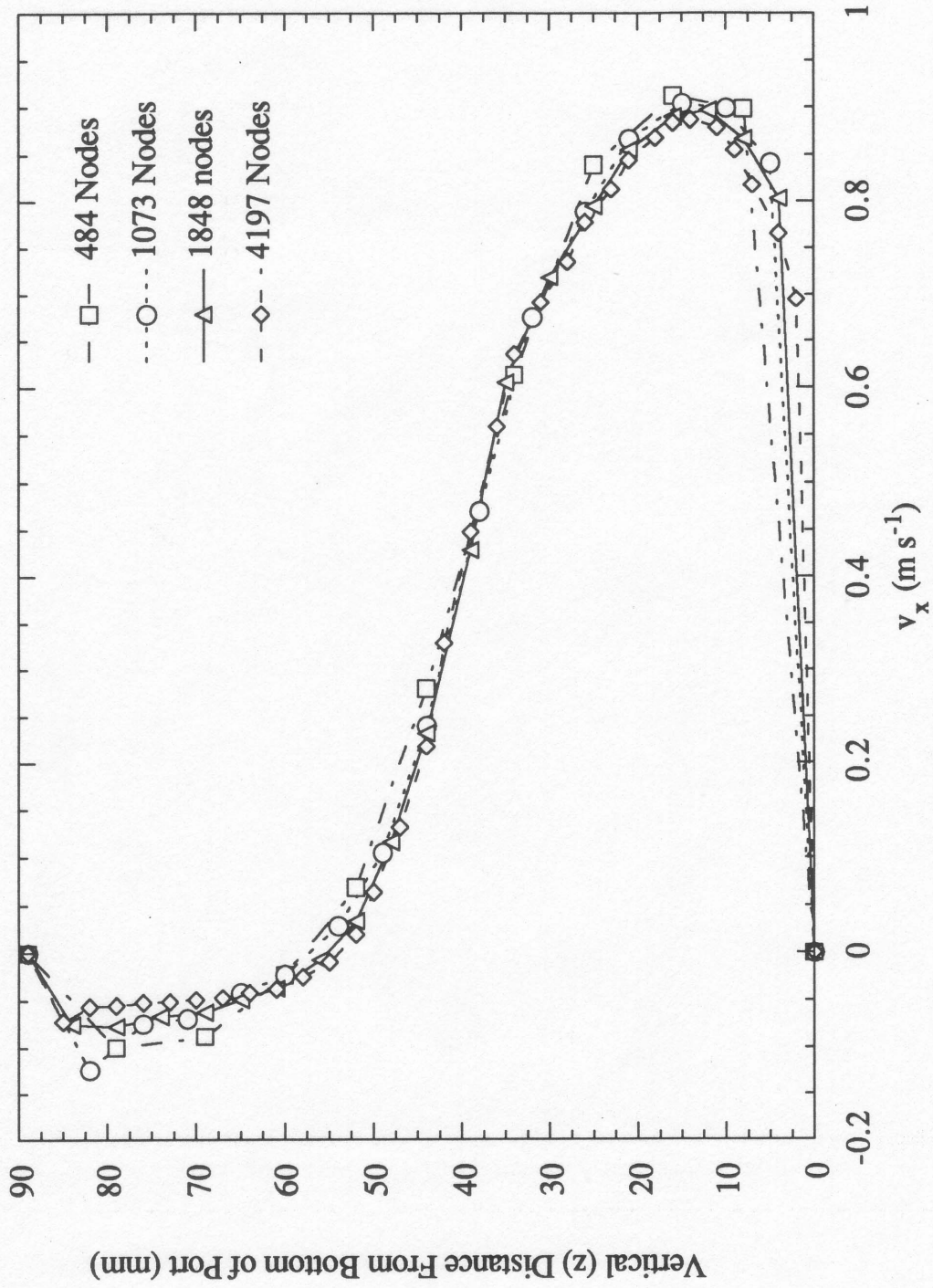


Figure 4. Effect of mesh density on x-velocity down nozzle outlet port (2-D simulation)

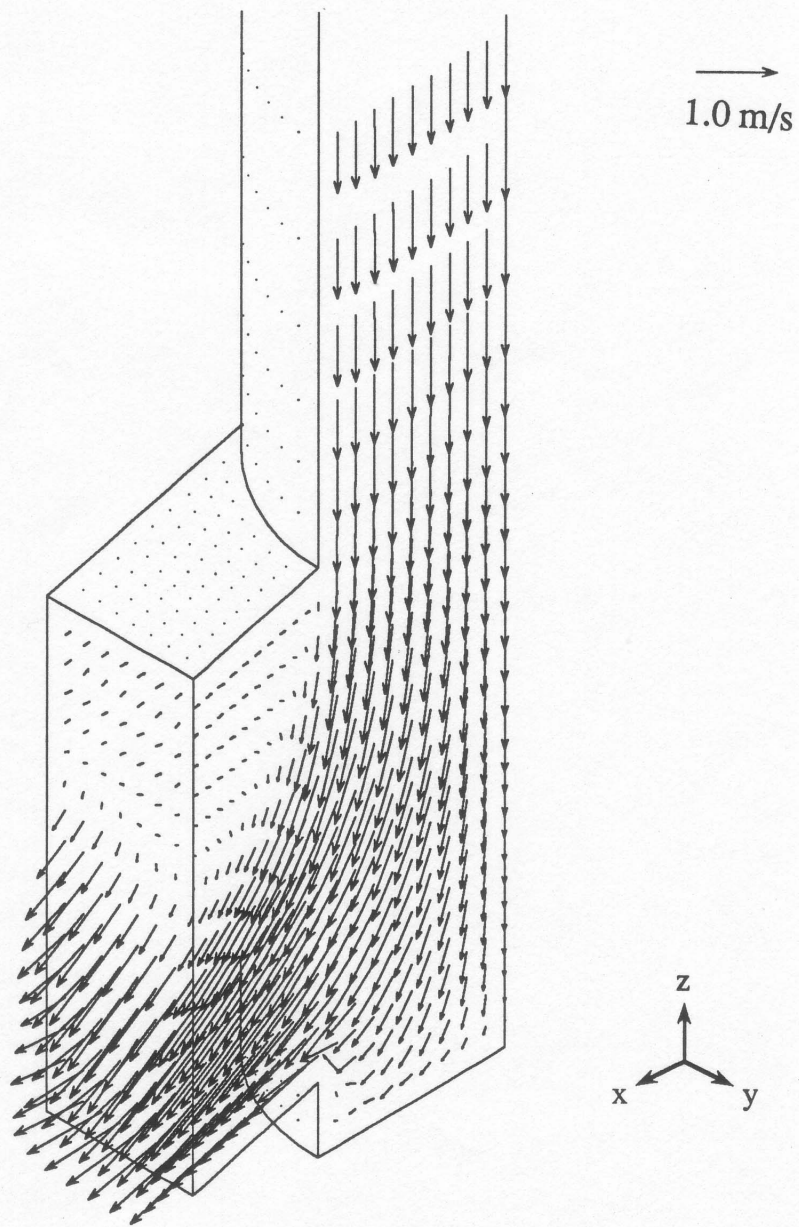


Figure 5. Calculated velocities in bottom portion of a 15° down SEN

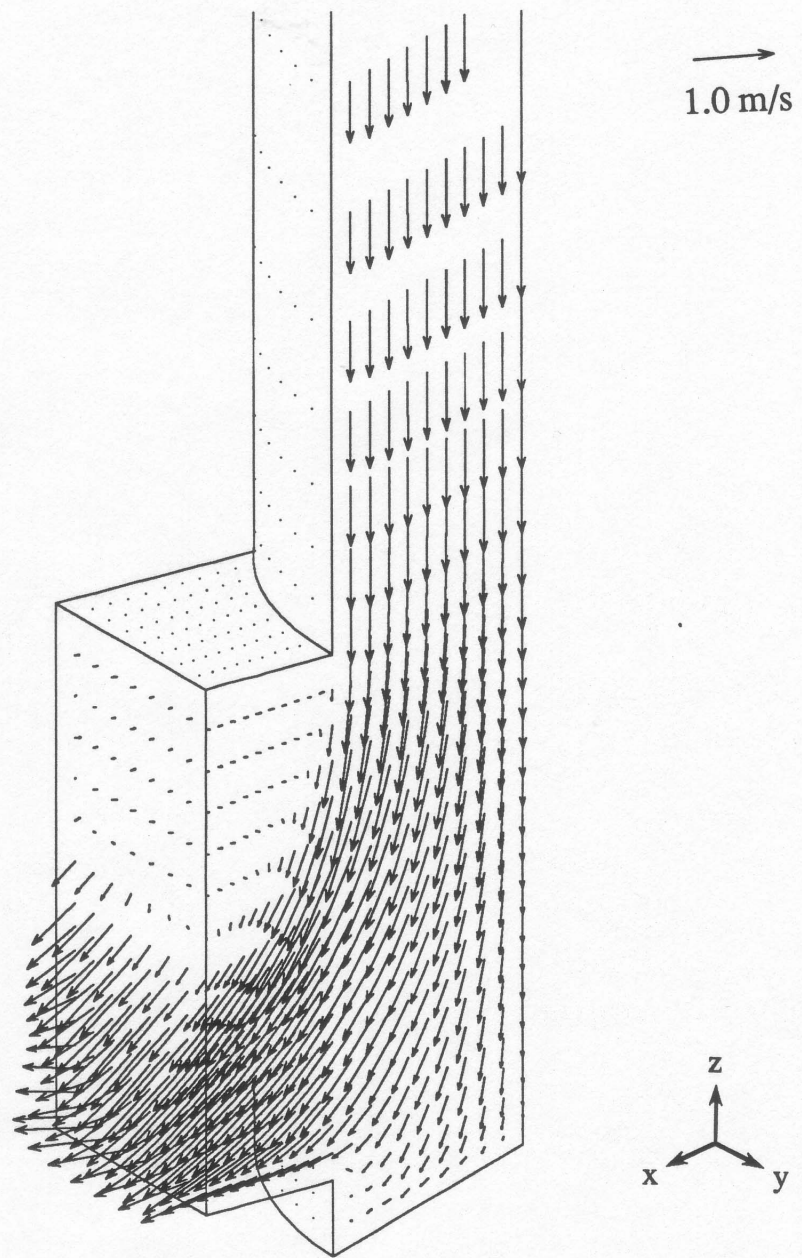


Figure 6. Calculated velocities in bottom portion of a 15° up SEN

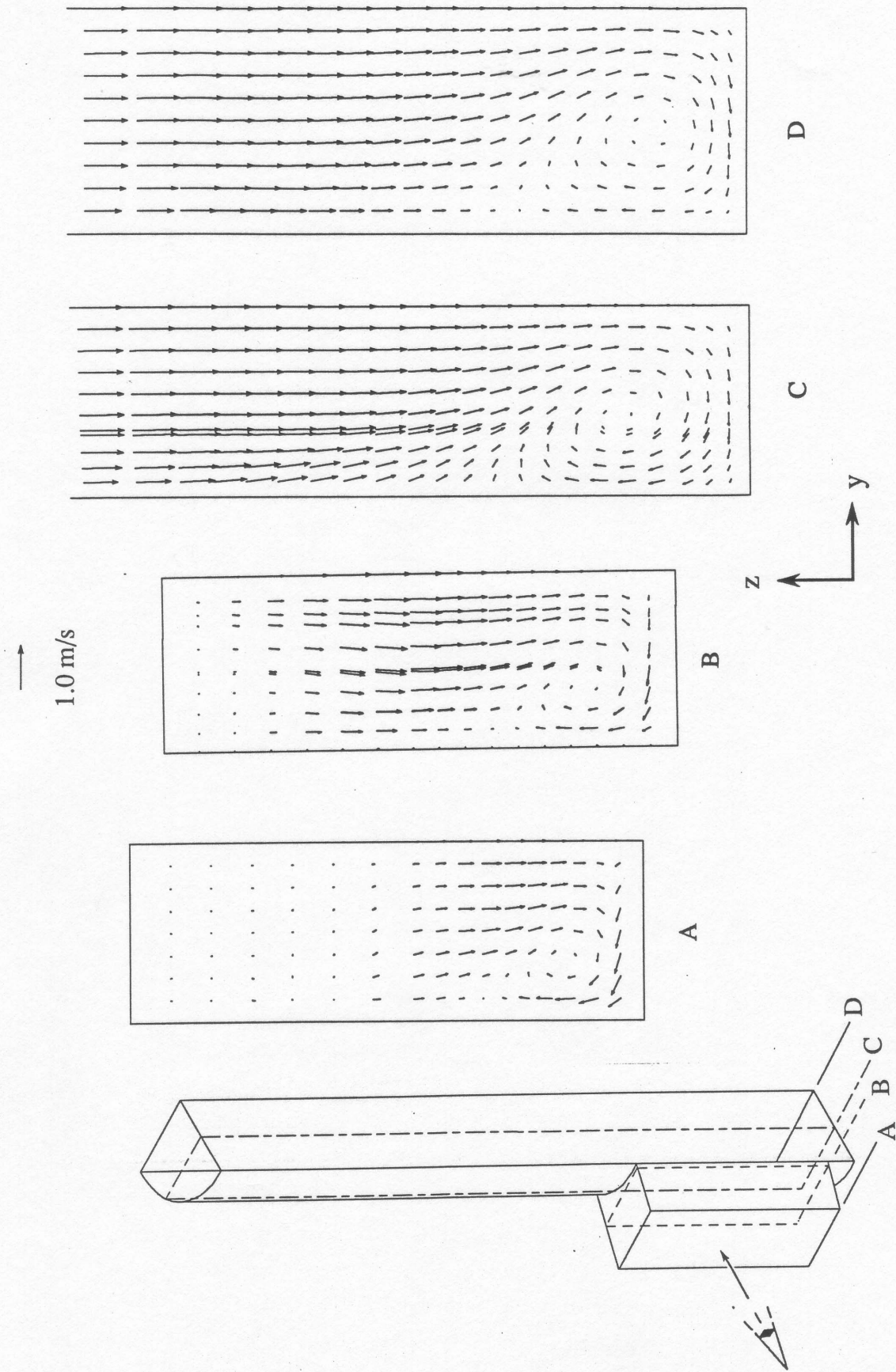


Figure 7. Calculated velocities in longitudinal sections through bottom of 15° up SEN.

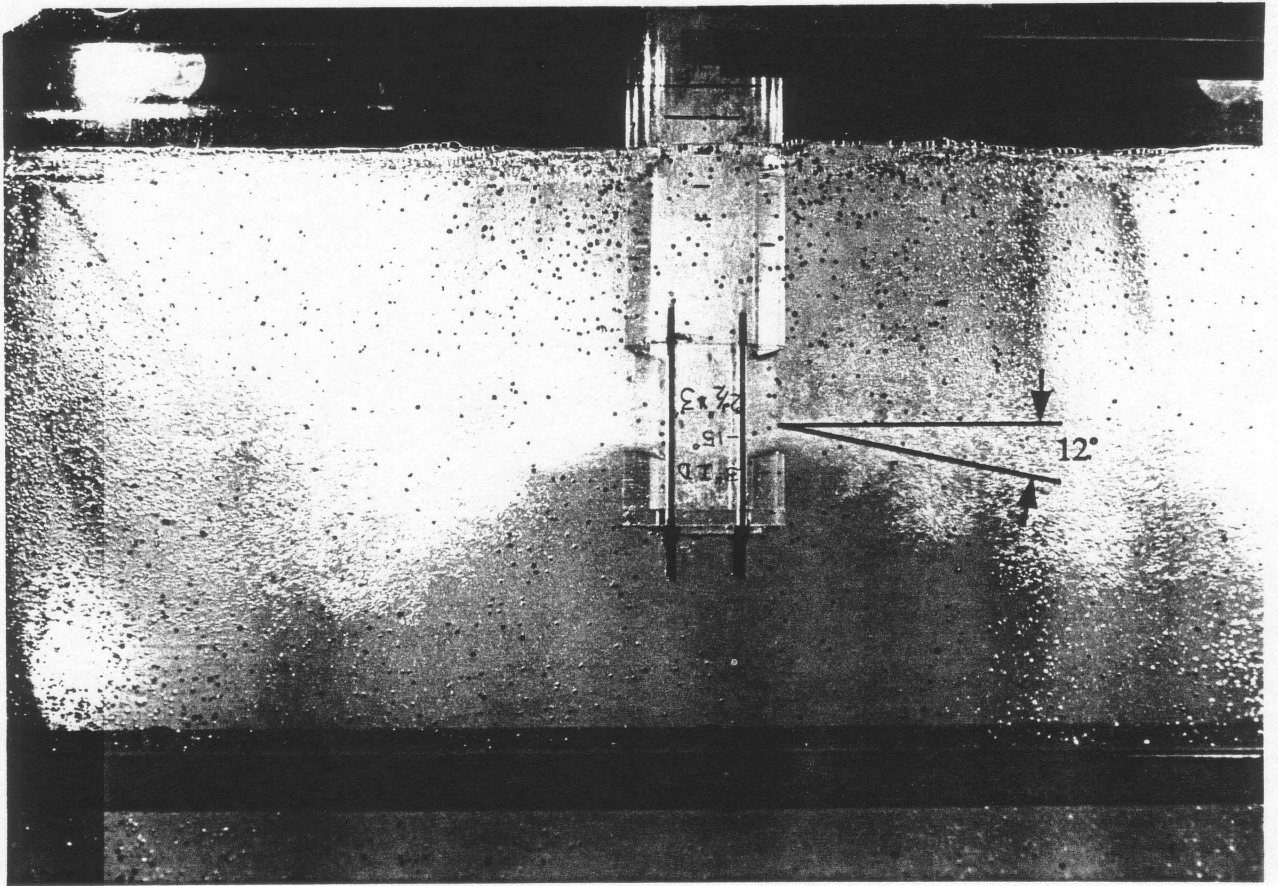
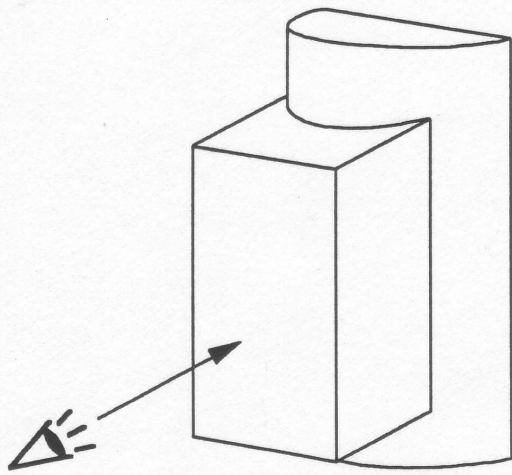
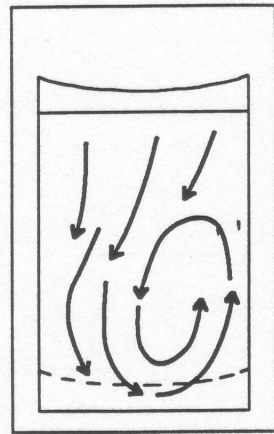


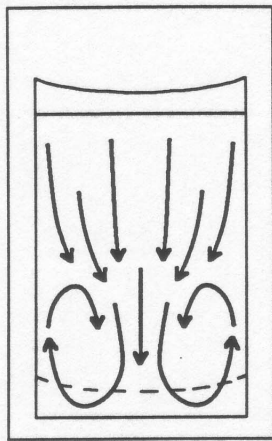
Figure 8. Flow pattern in water model using 15° up SEN



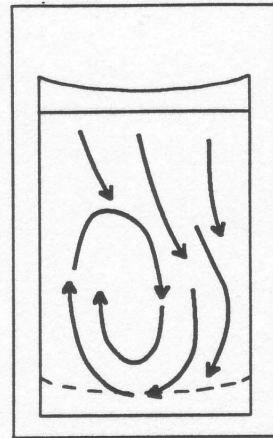
(a)



(c)



(b)



(d)

Figure 9. Typical flow patterns observed in port of SEN water model.<sup>29</sup>

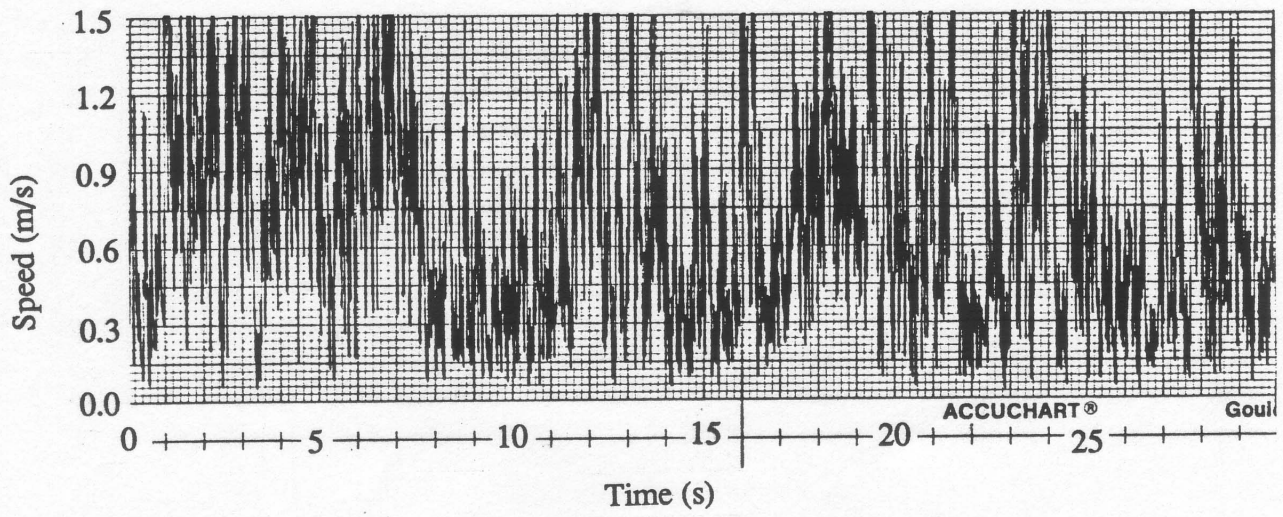


Figure 10. Recorded speed - time signal (100 mm from port outlet and 78 mm below top of port.)

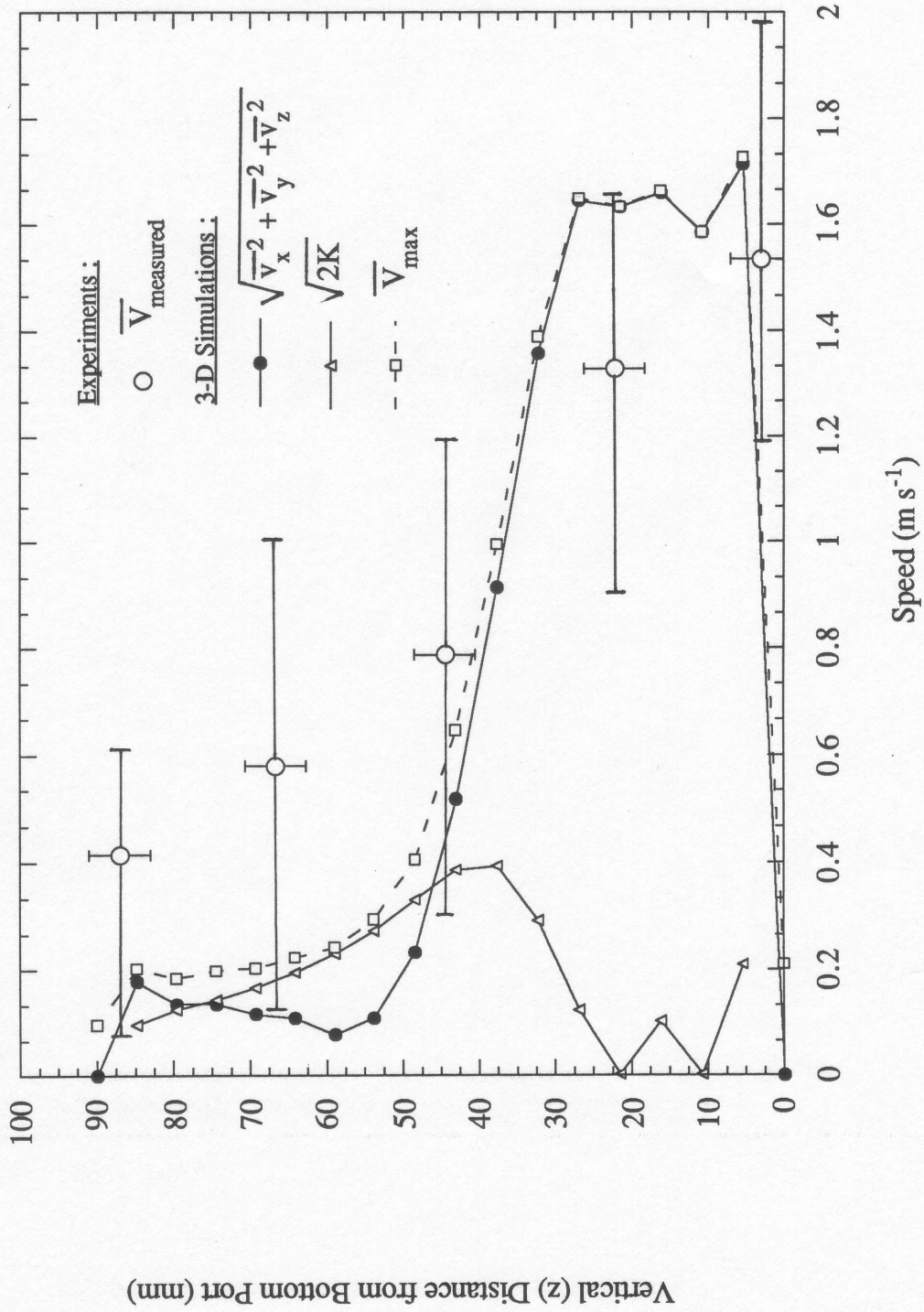


Figure 11. Comparison of experimental and predicted speed down centerline of SEN port exit (x-z plane)

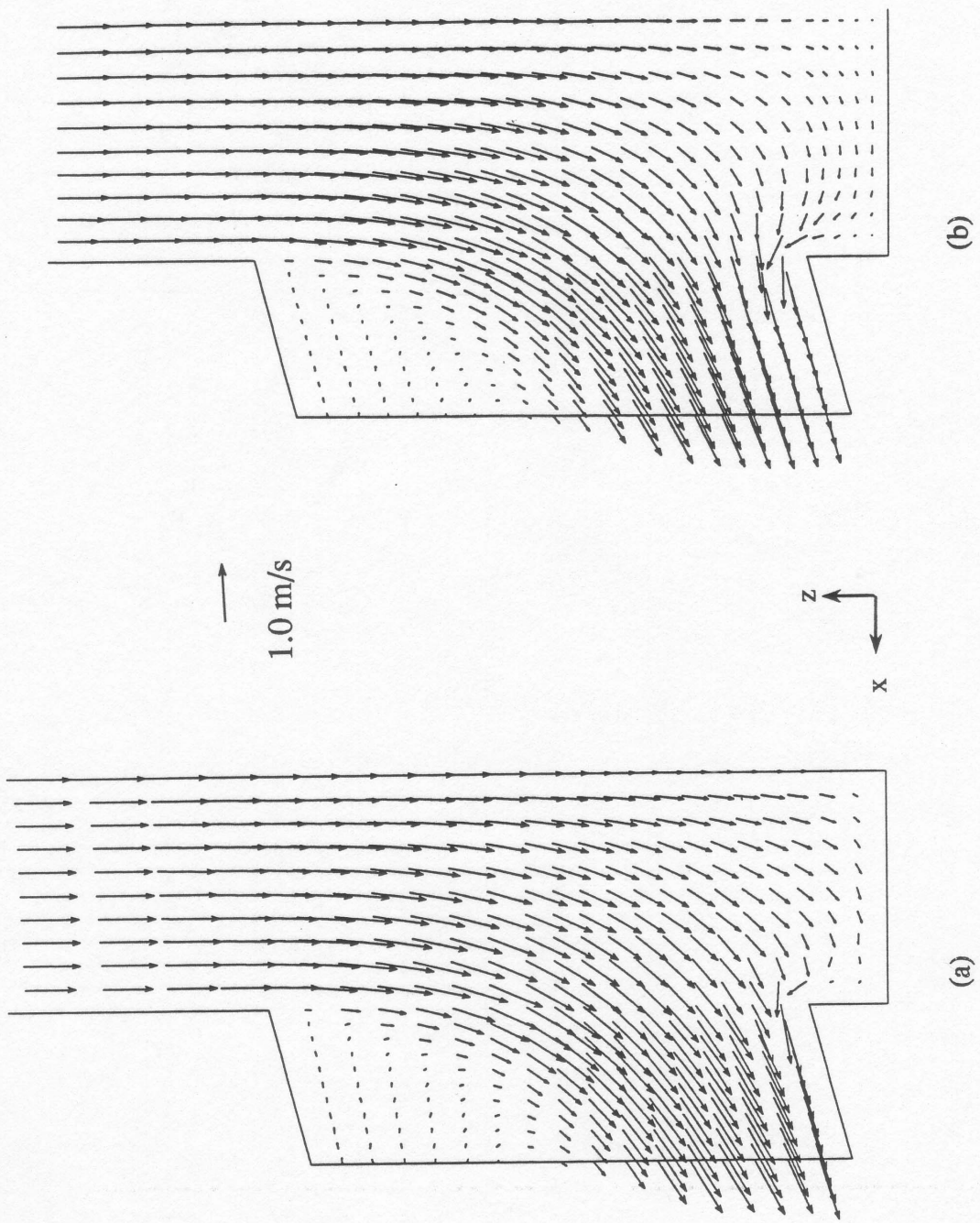


Figure 12. Calculated velocity fields at center plane of 15° down port  
 a) 3-D SEN model      b) 2-D SEN model

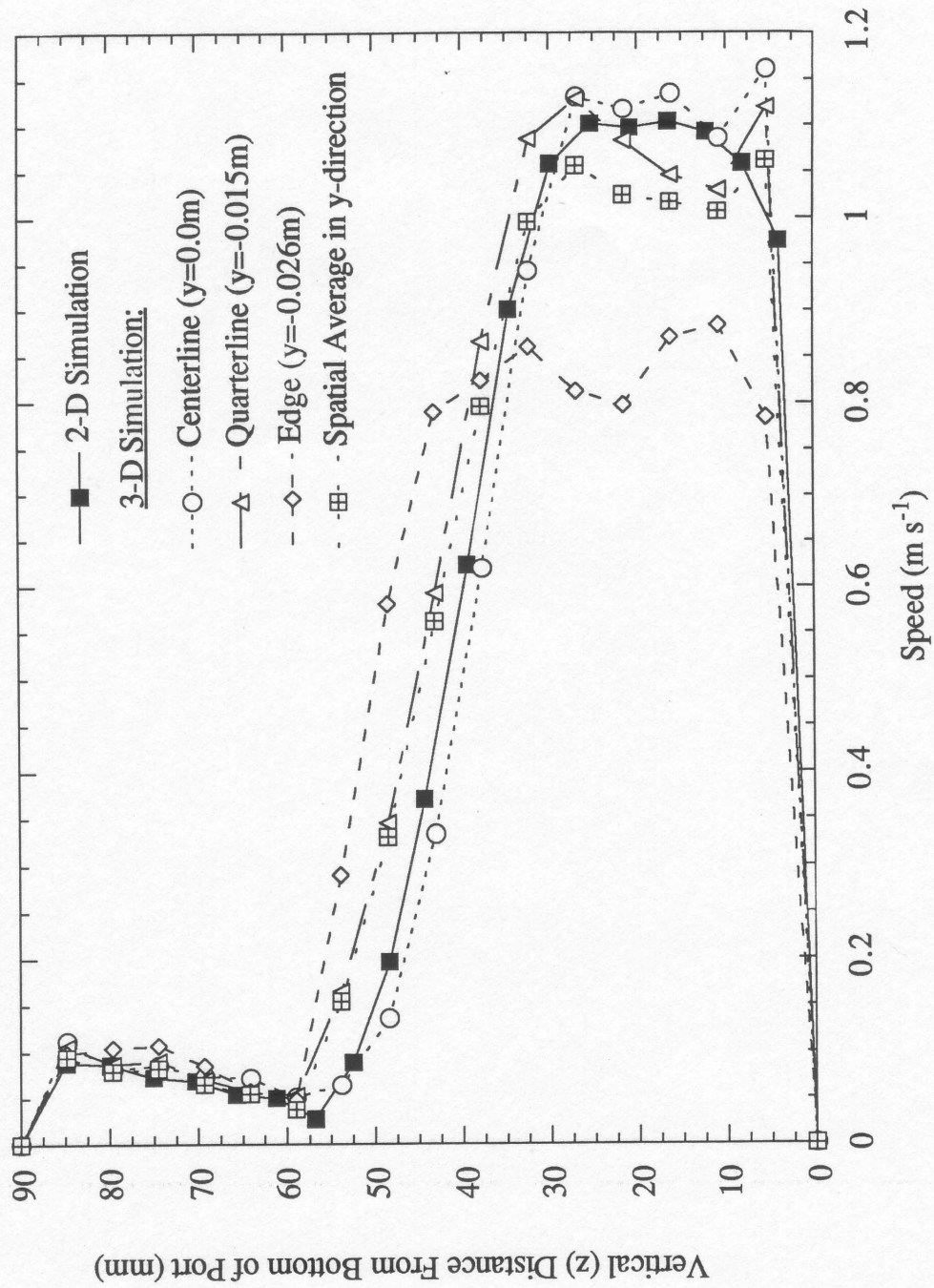


Figure 13. Comparison of jet speed down outlet port exit for 2-D and 3-D SEN simulations

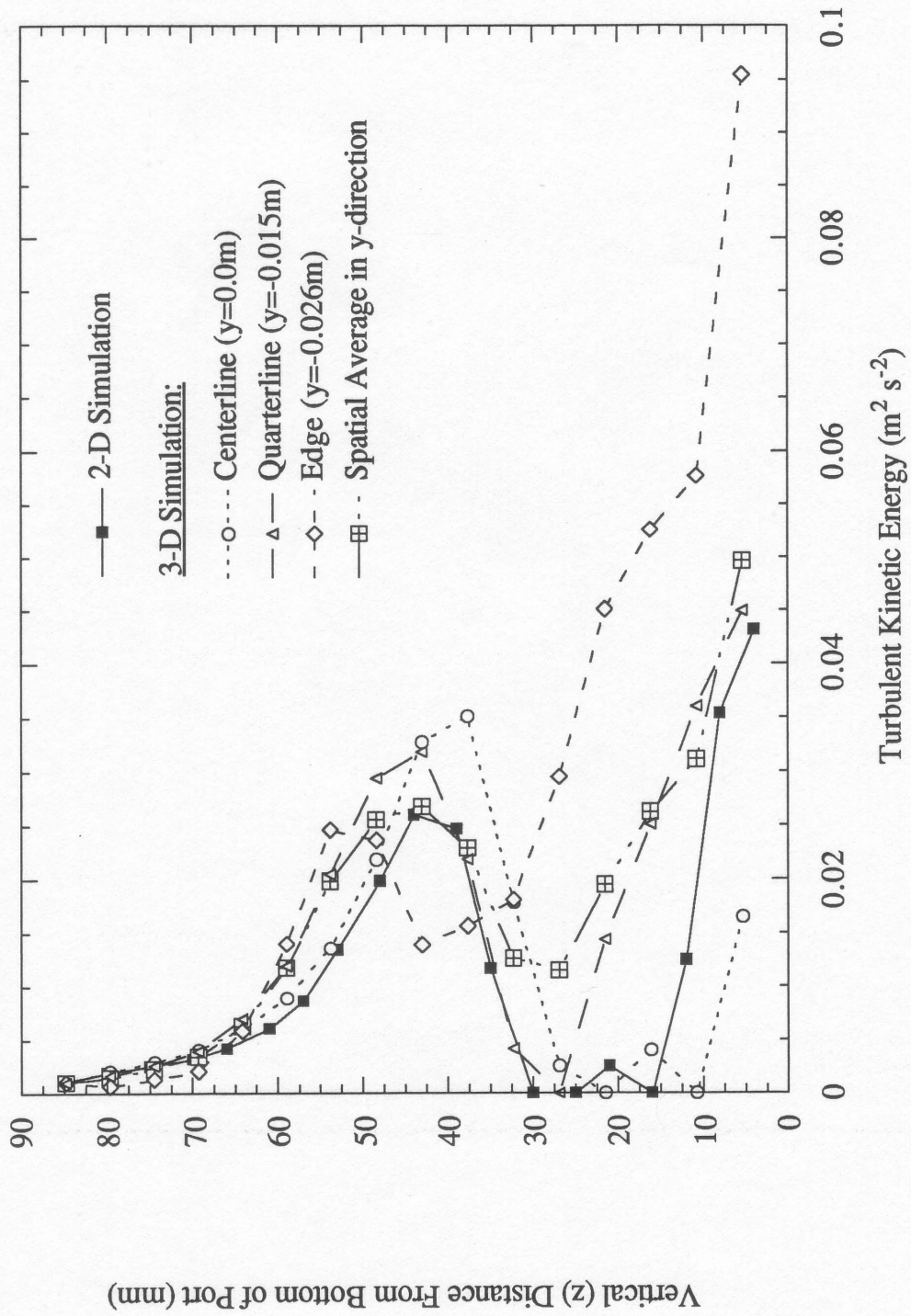


Figure 14. Comparison of turbulent kinetic energy down outlet port exit for 2-D and 3-D SEN simulations

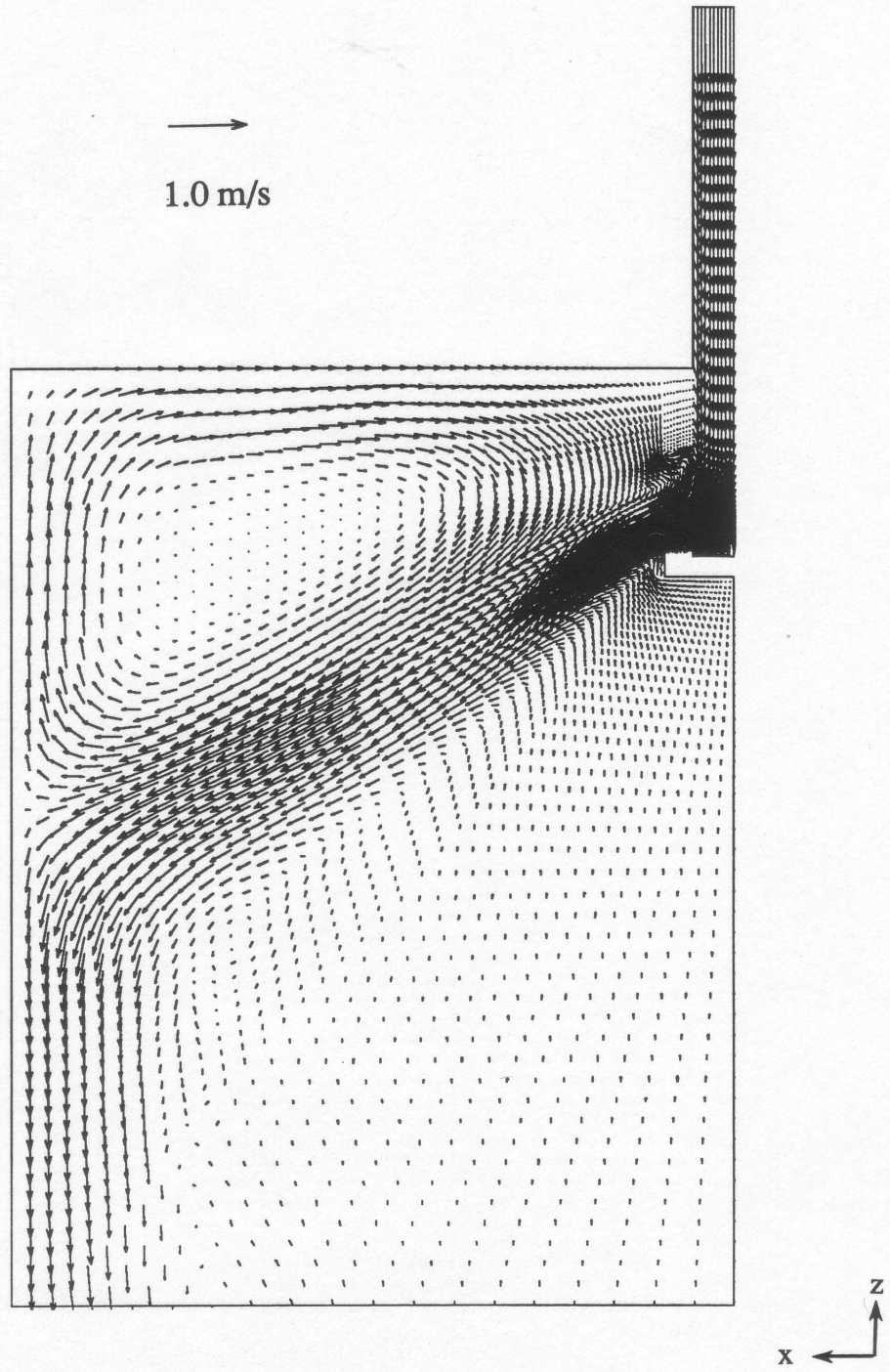


Figure 15. Calculated velocities in combined SEN / mold model (51 mm submergence depth)

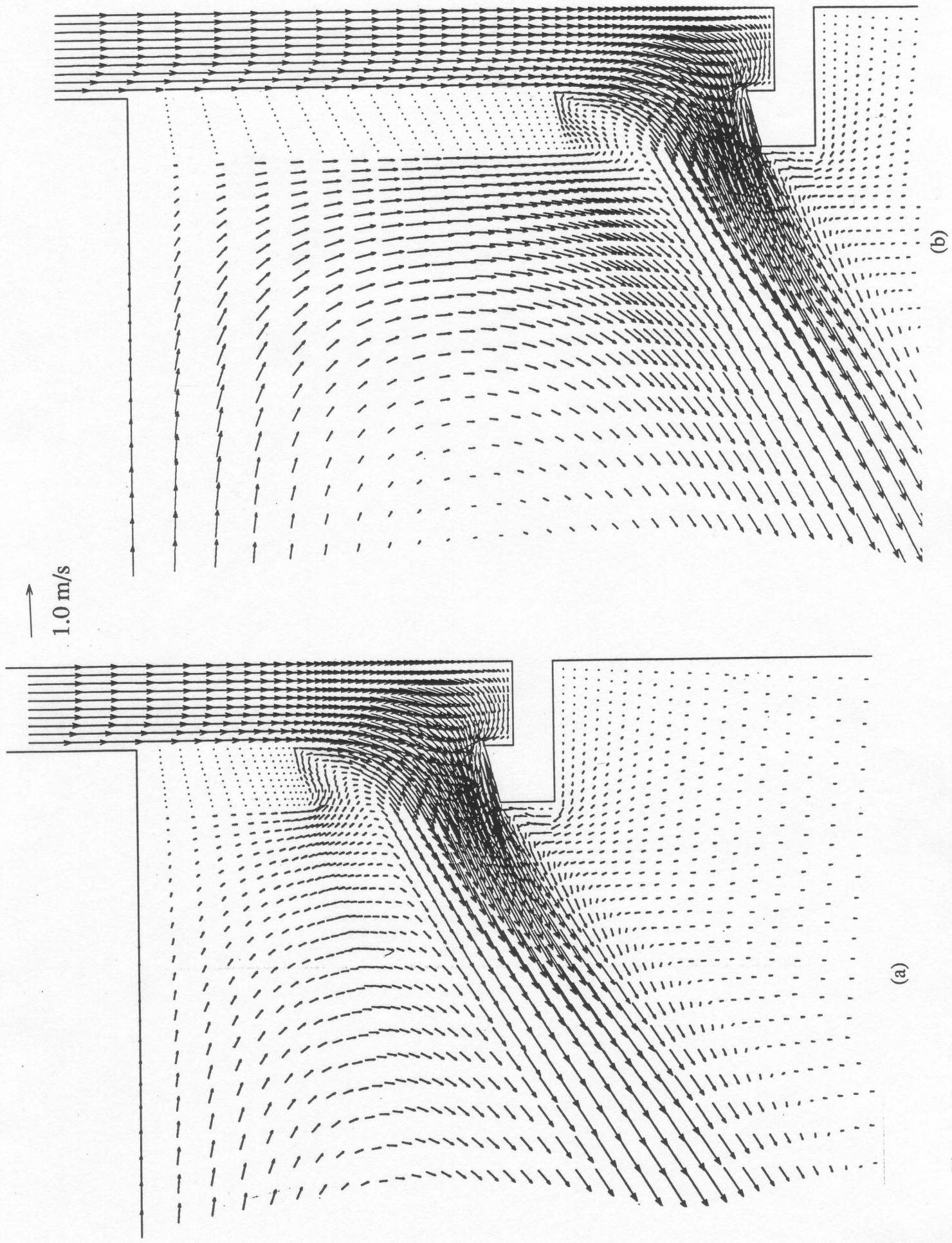


Figure 16. Calculated velocities near SEN port in combined SEN / mold model

a) 51 mm submergence depth      b) 203 mm submergence depth